AGU ADVANCING EARTH AND SPACE SCIENCE

Water Resources Research

RESEARCH ARTICLE
10.1029/2022WR032113

Key Points:

- Subgrid temperature distribution does not greatly affect basin-scale runoff but perturbs other water fluxes and their spatial variability
- Simulated 1 September snow water equivalent is more affected by subgrid temperature distribution in dry periods, without clear connections with elevation band width
- Temperature distribution is more relevant for grid cells with pronounced seasonality, low altitude, high-elevation ranges, and steep slopes

Supporting Information:

Supporting Information may be found in the online version of this article.

Correspondence to:

P. A. Mendoza,
pamendoz@uchile.cl

Citation:

Murillo, O., Mendoza, P. A., Vásquez, N., Mizukami, N., & Ayala, Á. (2022). Impacts of subgrid temperature distribution along elevation bands in snowpack modeling: Insights from a suite of Andean catchments. *Water Resources Research*, *58*, e2022WR032113. https://doi.org/10.1029/2022WR032113

Received 12 MAR 2022
Accepted 30 NOV 2022

Author Contributions:

Conceptualization: Octavio Murillo, Pablo A. Mendoza
Data curation: Octavio Murillo
Formal analysis: Octavio Murillo
Funding acquisition: Pablo A. Mendoza
Investigation: Octavio Murillo
Methodology: Octavio Murillo, Pablo A. Mendoza, Álvaro Ayala
Project Administration: Pablo A. Mendoza
Resources: Pablo A. Mendoza
Supervision: Pablo A. Mendoza, Nicolás Vásquez, Naoki Mizukami, Álvaro Ayala
Validation: Octavio Murillo, Pablo A. Mendoza, Nicolás Vásquez, Naoki Mizukami, Álvaro Ayala
Visualization: Octavio Murillo

Impacts of Subgrid Temperature Distribution Along Elevation Bands in Snowpack Modeling: Insights From a Suite of Andean Catchments

Octavio Murillo[1], Pablo A. Mendoza[1,2], Nicolás Vásquez[1], Naoki Mizukami[3], and Álvaro Ayala[4]

[1]Department of Civil Engineering, Universidad de Chile, Santiago, Chile, [2]Advanced Mining Technology Center (AMTC), Universidad de Chile, Santiago, Chile, [3]National Center for Atmospheric Research (NCAR), Boulder, CO, USA, [4]Centro de Estudios Avanzados en Zonas Áridas (CEAZA), La Serena, Chile

Abstract The implementation of elevation bands is a popular strategy to account for topographic heterogeneities in snowpack modeling. Here, we characterize the implications of subgrid temperature distribution along elevation bands through numerical experiments in nine mountainous basins of the Andes Cordillera, central Chile. Specifically, we analyze outputs from the Variable Infiltration Capacity model with six different setups: no elevation bands (i.e., flat grid cells; benchmark model) and elevation bands with vertical discretizations of 1,000, 750, 500, 200, and 100 m. The analyses are conducted in a wet period (April/1982–March/1987), dry period (April/2010–March/2015) and a climatological period (April/1982–March/2015). The results show that adding elevation bands yields little variations in simulated monthly or daily streamflow; however, there are important effects on the partitioning of precipitation between snowfall and rainfall, snowmelt, sublimation, and the spatial variability in 1 September snow water equivalent (SWE), suggesting a form of model-structure equifinality. Vertical temperature distribution generally yields less basin-averaged snowmelt and more (less) catchment-scale sublimation across water-limited (energy-limited) basins. Further, the implications of subgrid temperature distribution vary with the analysis period: fluxes are more affected during the wet period, while variations in 1 September SWE are more noticeable during the dry period. In general, the effects of topographic temperature distribution are reduced with increasing vertical discretization and can differ among catchments. Finally, the grid cells that yield the largest sensitivities to vertical discretization have relatively more humid conditions, large intra-annual variations in the water/energy budget, lower mean altitude, elevation ranges >1,000 m, and steep slopes (>15°).

Plain Language Summary Spatially distributed computer-based models are widely used to make predictions on water availability. In mountainous areas, it is common to distribute air temperature using elevation bands in modeling units with complex topography; however, the effects of the selected number of bands and/or elevation range on model results have not been assessed in detail. We use a suite of diverse Andean basins to document how the vertical distribution of air temperature along elevation bands affects the simulation of the water cycle at different spatial scales. Our results show that, although the incorporation of air temperature variability has little effects on the simulation of discharge at the basin outlets, similar results can arise from different spatial distributions of rainfall, snowfall, snowmelt, sublimation, and maximum annual accumulation. The implications of adding elevation bands may vary with the climate conditions (i.e., wet/dry) of the analysis period. Finally, we identify climate seasonality, mean altitude, elevation range, and slope as the key variables that should be examined carefully to decide where (i.e., which grid cells) the choice of elevation band configuration should be made with more caution.

1. Introduction

Snow is essential for water supply in mountain environments. In this context, numerical models are useful not only for understanding the physical processes that determine snow accumulation and melting (Clark et al., 2017; Lehning et al., 2006; Liston & Sturm, 1998) but also to make predictions that can be used for decision making (Schneider & Molotch, 2016), especially considering ongoing and future changes in climatic conditions (IPCC, 2021). Indeed, climate change is expected to impact mountain snowpack in many mountain regions of the world (Barnett et al., 2005), such as the Colorado Headwaters of USA (Rasmussen et al., 2014), the Appalachian

10.1029/2022WR032113

Writing – original draft: Octavio Murillo, Pablo A. Mendoza
Writing – review & editing: Nicolás Vásquez, Naoki Mizukami, Álvaro Ayala

Mountains (Demaria et al., 2016), the eastern Himalayas of Nepal (Bhatta et al., 2019), the extratropical Andes (Vicuña et al., 2021), and the Spanish Pyrenees (López-Moreno et al., 2013). Hence, improving the realism of snow models is critical for reliable estimates of snow water equivalent (SWE) under current and future climatic conditions.

Because water resources applications in mountainous areas require model simulations at the watershed or regional scales (Mendoza et al., 2020), spatial discretization strategies are needed to address heterogeneities within the domain of interest. Common choices involve the delineation of grid cells (e.g., Beck et al., 2020; Liang et al., 1996), subcatchments (e.g., Bandaragoda et al., 2004; Tesfa et al., 2014) and, more generally, hydrologic response units (e.g., Markstrom et al., 2008; Newman et al., 2014) as spatial modeling units. Subunit variability can also be incorporated in hydrologic modeling to improve the spatial representation of states and fluxes within each modeling element (e.g., Bajracharya et al., 2018; Hartman et al., 1999; L. Huang et al., 2022; Pradhanang et al., 2011) and to reduce the model sensitivity to changes in the spatial scale (Haddeland et al., 2002). Existing approaches include (a) "representative hillslopes" (e.g., Hazenberg et al., 2015; Swenson et al., 2019), which consists on identifying, for each modeling unit, hillslopes with a "typical" structure, dividing these into columns to represent lateral processes and (b) subgrid elevation bands (also referred to as "snow bands"; Hamman et al., 2018; Yeste et al., 2020), in which high-resolution topographic data are used to compute a hypsometric curve, and then discretize each modeling unit into elevation classes (e.g., Nijssen et al., 1997; Tesfa & Leung, 2017), where water and energy balances can be estimated.

Despite their simplicity, subgrid elevation bands are widely used in hydrologic and land surface modeling because they enable the incorporation of orographic effects on precipitation and temperature (Abdulla et al., 1996), improving the timing of simulated snowmelt (e.g., Habets et al., 1999; Vicuña et al., 2011) and streamflow dynamics (Abbaspour et al., 2007). However, the literature provides limited guidance for their implementation, based on the effects on simulated hydrological variables (Grusson et al., 2015). Indeed, many studies using elevation bands only provide information on the number of snow bands (e.g., Abdulla et al., 1996; Andreadis & Lettenmaier, 2006; Bajracharya et al., 2018; Li et al., 2017; Newman et al., 2017) or the vertical discretization (e.g., Arora et al., 2008; Fontaine et al., 2002; Haddeland et al., 2002), without further details and/or justification of their choice.

Only a few studies have examined the effects of elevation band configurations on hydrologic model simulations. Some of these have shown that a subunit discretization with elevation bands can yield similar domain-averaged SWE than that obtained with a gridded distributed model (Arola & Lettenmaier, 1996; Essery, 2003). Incorporating elevation bands may reduce domain-averaged peak SWE, decrease melt rates, and extend the snow cover duration in comparison to spatially lumped configurations (Clark et al., 2011; Essery, 2003). Such effects propagate toward simulated evapotranspiration (ET), with higher values when elevation bands are used (Grusson et al., 2015; Haddeland et al., 2002), and also on runoff timing (Haddeland et al., 2002; Hartman et al., 1999). The vertical distribution of precipitation and air temperature can also yield improvements in streamflow compared to the case without bands (Grusson et al., 2015), with marginal benefits beyond a certain number of elevation classes (Bhatta et al., 2019; Pradhanang et al., 2011).

To the best of our knowledge, no previous studies have systematically assessed the effects of subgrid elevation bands (specifically, the choice of vertical discretization) on hydrological portrayals in mountain environments, isolating the impact of temperature variability. Despite being very simple, distributing only air temperature with elevation within each modeling unit is a widely used strategy in hydrological modeling (e.g., Bohn et al., 2010; Clark et al., 2011; Hirabayashi et al., 2010; Kang et al., 2014; Minder et al., 2010; Nijssen et al., 2001; Younas et al., 2017), since it enables to incorporate the effects of subunit topographic variability on freezing levels and, therefore, on the partitioning of precipitation into rainfall and snowfall, which affects simulated hydrological states and fluxes. Hence, this paper addresses the following research questions:

1. How does subgrid temperature distribution along elevation bands affect simulated streamflow, catchment-scale water fluxes, and SWE near the date of maximum accumulation?
2. What are the implications of adding elevation bands on simulated SWE at the grid cell scale?
3. What attributes characterize those grid cells where representing subgrid temperature variability makes a large difference in simulated SWE?

To seek for answers, we configure the Variable Infiltration Capacity (VIC; Liang et al., 1994, 1996) macroscale hydrological model in nine basins located along the western slopes of the extratropical Chilean Andes. We compare simulation results from a calibrated model with flat grid cells (benchmark) against alternative model configurations considering vertical discretizations defined every 1,000, 750, 500, 200, and 100 m. In the latter configurations, only air temperature is distributed with elevation, while precipitation rates and the rest of meteorological forcings are assumed to be spatially constant in each grid cell. We select the VIC model given: (a) the global interest of users (Addor & Melsen, 2019; Sepúlveda et al., 2022), especially for snow hydrology studies (Andreadis et al., 2009; Chen et al., 2014; Houle et al., 2017; Islam et al., 2017; Li et al., 2017; Livneh & Badger, 2020; Marshall et al., 2019; Mote et al., 2005; Xiao et al., 2021), and (b) past and ongoing efforts to characterize the current and future hydrology across continental Chile (DGA, 2017; Vásquez et al., 2021; Vicuña et al., 2021). To disentangle the possible role of climatic conditions on intermodel differences, and partially motivated by the negative effects of the ongoing megadrought in central Chile (Garreaud et al., 2017, 2019), we conduct our assessments for a climatological period (April/1982 to March/2015), a wet period (April/1982 to March/1987), and a dry period (April/2010 to March/2015). Overall, the results presented here shed light on the state variables and fluxes that are most affected, and the type of modeling unit where it is critical to explicitly incorporate subgrid temperature distributions.

2. Study Domain

We conduct our analyses in nine mountainous basins located along the western slopes of the extra-tropical Andes Cordillera (32.5°–37°S, 70°–71.5°W, Figure 1). These basins were selected based on the following criteria: (a) a near-natural flow regime defined as a maximum threshold value of 5% for the relationship between annual volume of water assigned for permanent consumptive use and the mean annual flow (Table 3 in Alvarez-Garreton et al., 2018), (b) absence of large reservoirs within each catchment, and (c) small (<2%) glacierized area. Furthermore, these catchments span a wide range of hydroclimatic conditions (Table 1), from high aridity index (2.9) and relatively low mean annual precipitation (486 mm; Estero Pocuro en el Sifón) to low aridity index (0.7) and high mean annual precipitation (1,929 mm; Río Ñuble en La Punilla). The southern basins (35°–37°S in Figure 1) also have larger vegetation coverage (just forest fraction coverage shown) due to the lower aridity and increased precipitation, providing higher runoff ratios.

Despite snow being a key component of the water cycle in all case study basins, these encompass different hydrological regimes. This is illustrated in Figure 1 (left and right panels), including catchment-scale precipitation and monthly averages of hydrologic variables simulated with the VIC model. Three dominant regimes can be seen: (a) rainfall-driven (Pocuro), with peak discharge values corresponding to months where precipitation events typically occur (April–September); (b) snow-dominated (Las Leñas), with peak discharge due to spring and summer snowmelt (October–March); and (c) mixed regimes characterized by two peaks in mean monthly runoff. The latter hydrological regimes can be further stratified into (a) pluvio-nival, where rainfall is the main control for runoff production (Claro), (b) fully mixed, with comparable rainfall and snowmelt-driven peak monthly runoff (Ñuble), or (c) nivo-pluvial, with snowmelt dominating catchment-scale hydrology (Arrayán, Mapocho, Colorado, Palos, and Melado). The reader is referred to Baez-Villanueva et al. (2021) for further details on the classification criteria used here for hydrological regimes. Interestingly, there are catchments where the seasonal cycles of soil moisture and runoff are similar, regardless of their hydrological regimes (Las Leñas, Colorado, Palos, and Melado), and basins where these cycles are different (Arrayán, Mapocho, Claro, and Ñuble).

3. Data and Methods

3.1. Meteorological Forcings and Streamflow Data

Daily precipitation and temperature extremes are obtained from an updated version of the CR2MET data set (Boisier et al., 2018), which has a horizontal resolution of 0.05° × 0.05°, covering continental Chile for the 1979–2016 period. The data set for precipitation was generated with a statistical postprocessing technique that uses topographic descriptors and large-scale climatic variables (water vapor and moisture fluxes) from ERA-Interim (Dee et al., 2011) and ERA5 (C3S and Copernicus Climate Change Service [C3S], 2017) as predictors and observed daily precipitation from gauge stations as predictand. For the case of maximum and minimum daily temperature, additional variables from MODIS land surface products were added as predictors. Daily

10.1029/2022WR032113

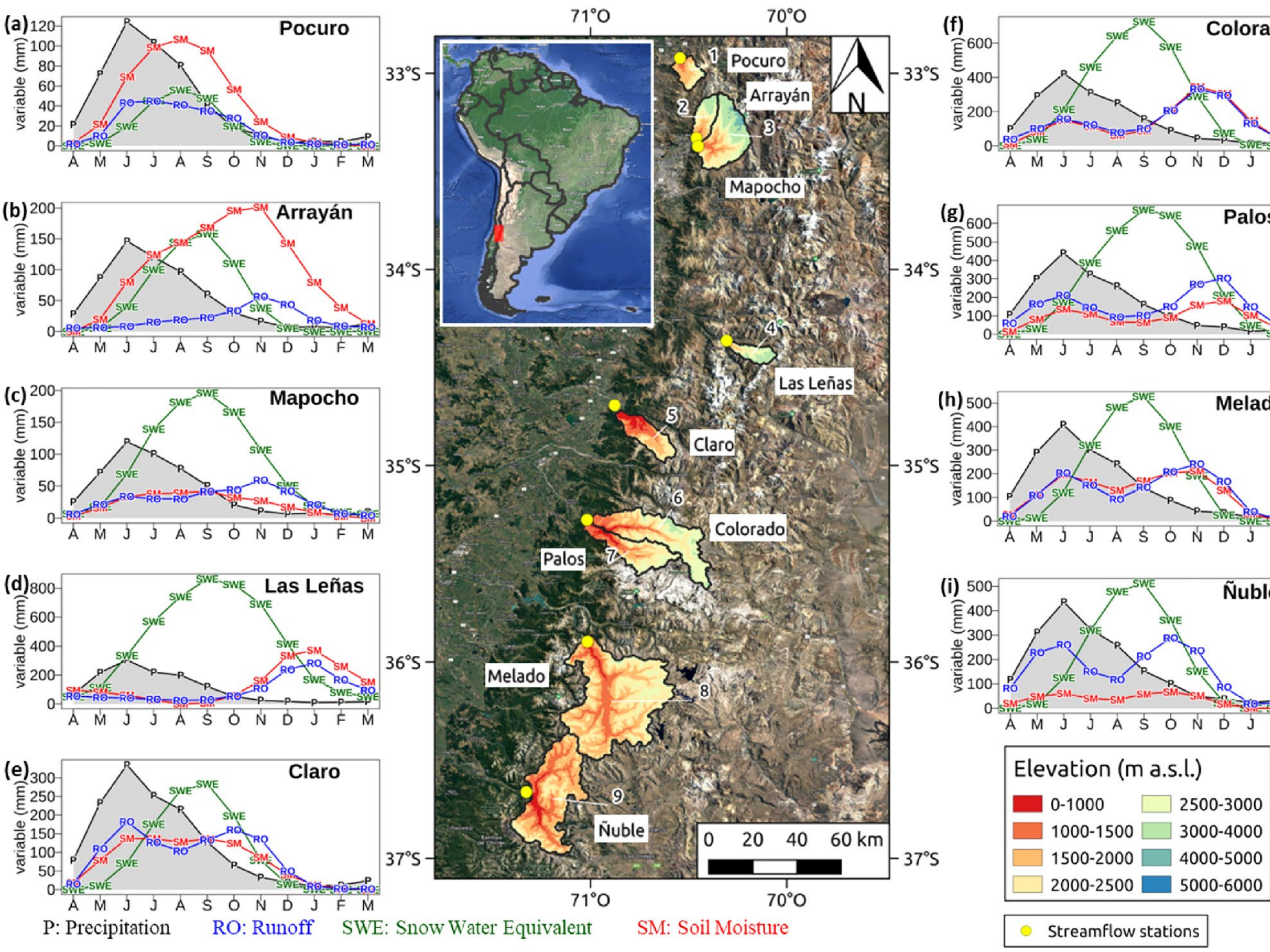

Figure 1. Location and elevation of the nine case study basins (center panel), along with seasonal cycles with precipitation and simulated water balance variables (left and right panels) during a climatological period (April/1982 to March/2015) for the nine case study basins: (a) Estero Pocuro en el Sifón, (b) Estero Arrayán en la Montosa, (c) Río Mapocho en Los Almendros, (d) Río Las Leñas antes junta Río Cachapoal, (e) Río Claro en El Valle, (f) Río Colorado en junta con Palos, (g) Río Palos en junta con Colorado, (h) Río Melado en el Salto, and (i) Río Ñuble en La Punilla. For modeled soil moisture, we subtract the lowest mean monthly value of the year so that the plotted values show only the active range of variation.

precipitation and temperature time series are disaggregated into 3-hourly time steps using the subdaily distribution provided by ERA-Interim. Relative humidity and wind speed are derived for the same horizontal resolution grid by spatially interpolating a blend between ERA-Interim and ERA5 data sets, because the latter was not available for the entire study period (1985–2015) at the moment of data acquisition (early 2018). Despite the short temporal coverage from ERA5 (2010–2016), the updated reanalysis information was included for a better spatial representation of the mega drought (Garreaud et al., 2019; Vicuña et al., 2021), and possible temporal inconsistencies with Era-Interim were addressed through linear regression models between daily variables obtained from both products (not shown). Shortwave and longwave radiation are estimated at each grid cell using the empirical algorithms in the Mountain Microclimate Simulation Model (MTCLIM; Bohn et al., 2013; Hungerford, 1989), which is implemented in the VIC model.

Streamflow data are obtained from stations maintained by the Chilean Water Directorate (DGA, available from the CR^2 Climate Explorer https://www.cr2.cl/datos-de-caudales/).

3.2. Hydrological Model

VIC is a macroscale, process-based, and semidistributed hydrologic model. Our VIC modeling unit is the grid cell, which is defined here to match the meteorological forcing data resolution (i.e., $0.05° \times 0.05°$). Interception is simulated with a one-layer canopy reservoir that is emptied by canopy evaporation, transpiration, or throughfall,

Table 1
List of Catchment Attributes

Catchment	Latitude[a] (°)	Longitude[a] (°)	Area (km²)	Mean basin elevation and range (m a.s.l.)	Mean slope (°)	Mean annual precipitation (mm/year)	Mean annual AI (PET/*P*)	Mean annual runoff (mm/year)	Mean annual runoff ratio (*Q*/*P*)	Forest fraction (%)
Estero Pocuro en el Sifón	−32.92	−70.54	181	2,107 (1,002–3,695)	22.1	486	2.9	126	0.26	0.2
Estero Arrayán en la Montosa	−33.33	−70.46	216	2,469 (969–3,833)	24.2	615	2.4	233	0.38	0.4
Río Mapocho en Los Almendros	−33.37	−70.45	638	2,936 (970–5,428)	25.2	503	2.5	310	0.62	0.4
Río Las Leñas antes junta Río Cachapoal	−34.36	−70.31	172	2,865 (1,279–4,574)	30.4	1,266	1.1	752	0.59	0.2
Río Claro en El Valle	−34.69	−70.87	349	1,596 (535–3,334)	22.2	1,422	0.9	862	0.61	27.1
Río Colorado en junta con Palos	−35.28	−71.00	877	2,253 (594–4,073)	19.6	1,802	0.8	1,387	0.77	11.5
Río Palos en junta con Colorado	−35.27	−71.02	490	2,013 (595–4,037)	19.9	1,891	0.7	1,689	0.89	16.7
Río Melado en el Salto	−35.88	−71.02	2,127	2,010 (698–3,619)	23.5	1,766	0.8	1,232	0.70	1.9
Río Ñuble en La Punilla	−36.66	−71.32	1,254	1,711 (566–2,617)	23.9	1,929	0.7	1,718	0.89	13.6

Note. Hydrologic variables correspond to the period April/1979 to March/2015. Mean slope and forest fraction were obtained from Alvarez-Garreton et al. (2018). AI, PET, *P*, and *Q* denote aridity index, mean annual potential evapotranspiration, precipitation, and total runoff, respectively.
[a]These coordinates are associated with the catchment outlet.

which occurs when additional precipitation exceeds the storage capacity of the canopy. Each grid cell has three soil layers: the two upper layers represent the interaction between soil moisture and vegetation, while the bottom layer simulates baseflow processes. It should be noted that VIC does not represent terrain-driven lateral flow nor considers lateral exchange of fluxes between grid cells, which implies that water can only enter a grid cell from the atmosphere. A two-layer energy balance model is used to simulate snowpack dynamics: the upper layer solves the energy balance between the atmosphere and the snowpack, and the bottom layer stores the excess snow mass from the upper layer (Andreadis et al., 2009; Cherkauer & Lettenmaier, 2003).

In VIC, different vegetation classes are allowed through a mosaic approach, where water and energy balance terms are computed independently for each land cover class. Subgrid variability in topography can be incorporated through elevation bands, using their mean elevations to lapse grid-averaged values of temperature and/or precipitation. In such case, the model assumes that the same soil type, vegetation classes, and fractional areas that were originally assigned to flat grid cells are preserved for each band. Hence, the snow model is run at each land cover/elevation tile separately, and the simulated water and energy states and fluxes are spatially averaged to obtain grid cell or elevation band estimates (Andreadis et al., 2009). Although increasing the number of elevation bands increases the computational cost, it can potentially improve the spatial representation of temperature and hydrologic model simulations.

Figure 2 illustrates how VIC represents topographic variability through elevation bands, and how these can be configured. It can be noted that the model lumps all areas within the same elevation range into one band and hence does not explicitly consider other topographic features such as slope or aspect in process representations. Therefore, subgrid topographic heterogeneities in each modeling unit are approximated by hypsometric curves, whose accuracy depends on the vertical discretization selected. This implies that, if fixed elevation band widths are used, very similar curves can be achieved beyond a specific vertical discretization (see example in Figure S3 in Supporting Information S1).

3.3. Experimental Setup

3.3.1. Benchmark Model

To assess the effects of subgrid temperature distribution along elevation bands on simulated states and fluxes, we compare VIC simulations with different elevation band implementations against a benchmark model based on the work by Vásquez et al. (2021). In such implementation, a priori distributions for vegetation parameters were

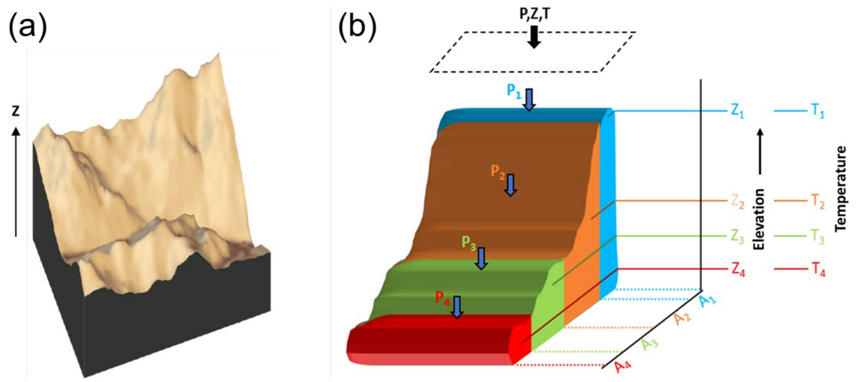

Figure 2. Spatial representation of subgrid topographic variability in VIC. The terrain heterogeneities obtained from 30-m resolution DEMs in each grid box (a) are approximated through elevation bands (b), where *A*, *P*, *T*, and *Z* denote area, average precipitation, air temperature, and terrain elevation for each band, respectively.

obtained using the land cover classes described in Zhao et al. (2016); spatial information on hydraulic conductivity values was obtained from the Natural Resources Data Center (CIREN for its acronym in Spanish) and all grid cells were considered flat (i.e., no elevation bands are defined). In our setup, all model simulations are conducted in full energy balance mode—dismissing frozen soil processes—and no horizontal runoff routing is performed since, for the contributing catchment areas examined here, routing effects are not expected to be important at the daily or longer time scales (Beck et al., 2020; Gericke & Smithers, 2014). Therefore, modeled streamflow is obtained from basin-averaged runoff.

The parameters for the benchmark model (Table 2) are calibrated using the Shuffled Complex Evolution global optimization algorithm (Duan et al., 1993) and streamflow data observed at each catchment outlet (see Section 3.1). All soil parameters are considered spatially constant within each catchment (i.e., no parameter regularization was performed). The objective function is the Kling-Gupta efficiency (KGE) metric (Gupta et al., 2009):

$$\mathrm{KGE} = 1 - \sqrt{(r-1)^2 + (\alpha-1)^2 + (\beta-1)^2} \tag{1}$$

Table 2
List of VIC Parameters and Limits Considered for Calibration

			Calibration range	
Parameter	Description	Units	Min	Max
infilt	Variable infiltration curve parameter (b_{infilt})	–	0.001	0.162
D_s	Fraction of $\mathrm{Ds}_{\mathrm{max}}$ where nonlinear baseflow begins	–	0.312	0.806
$\mathrm{Ds}_{\mathrm{max}}$	Maximum velocity of baseflow	mm/day	83.2	183.2
W_s	Fraction of maximum soil moisture where nonlinear baseflow occurs	–	0.108	0.900
C	Exponent used in baseflow curve	–	3.0	10.9
depth_1	Thickness of each soil moisture layer	m	0.014	2.169
depth_2		m	0.418	5.281
depth_3		m	0.173	3.753
K_{sat}	Saturated hydraulic conductivity	mm/day	1,499	2,565
Newalb	Fresh snow albedo		0.725	0.950
$\mathrm{Alb}_{\mathrm{acum\ a}}$	Snow albedo curve parameter	–	0.725	0.950
$\mathrm{Alb}_{\mathrm{thaw\ a}}$	Snow albedo curve parameter	–	0.883	0.920
T_{rain}	Minimum temperature for rainfall occurrence	°C	−2.735	3.446
r_{snow}	Snow surface roughness	m	1.24E−5	0.022

where r is the Pearson correlation coefficient between simulated and observed runoff; α is the ratio of the standard deviation of simulated values to the standard deviation of observed values; and β is the ratio between the mean of the simulated values to the mean of observations.

The calibration process considers streamflow data for at least 4 years within the period April/1990 to March/2010, and if the minimum record length is not satisfied, the periods April/1985 to March/1990 and April/2010 to March/2015 are considered. All model simulations are conducted at 3-hourly time steps for the period January/1979 to December/2015, using the first 3 years to initialize model states. If two or more parameter sets yield the same KGE values, we select the one that maximizes the Nash-Sutcliffe efficiency (NSE; Nash & Sutcliffe, 1970). We do not use any other data sets than streamflow to assess model performance, and the same parameter sets found in this step are used for the modeling experiments with subgrid elevation bands described in Section 3.3.2.

3.3.2. Alternative Model Configurations

For each basin, we create five alternative model configurations by spatially disaggregating grid cells into elevation bands with fixed intervals. We use the following vertical discretizations because they span a reasonable range of options considered in previous studies: 1,000 m (e.g., Tesfa & Leung, 2017 in high-elevation areas), 500 m (e.g., M. Huang et al., 2013; Nijssen et al., 1997), 200 m (e.g., Haddeland et al., 2002; Hartman et al., 1999), and 100 m (e.g., Clark et al., 2011; Ragettli et al., 2014). Additionally, we include a 750-m vertical discretization to assess an intermediate option between 500- and 1,000-m configurations. To delineate elevation bands, we use the 30-m Advanced Spaceborne Thermal Emission and Reflection (ASTER) Global Digital Elevation Model (GDEM) version 2 (Tachikawa et al., 2011). To harmonize all these spatial configurations, we consider 0 m a.s.l. as the starting point of elevation bands for all catchments, instead of the lowest point of each catchment's grid cell; hence, the same elevation classes are used to discretize all grid cells, regardless of their individual elevation ranges (similar to the global method used by Tesfa & Leung, 2017). We choose this type of configuration to facilitate future development and comparisons of SWE simulations between grid cells and elevation bands located in different basins across continental Chile. For the lowest and the highest elevation bands in each grid cell, we set a minimum fractional area of 5% (with respect to the grid cell's area); if such a condition is not met, that band (i.e., the lowest and/or the highest) is merged to the closest one. This implies that peak elevations may be excluded from our representation of subgrid variability.

In all alternative model configurations, precipitation rates are assumed to be constant with elevation to focus our attention on the potential effects of subgrid temperature variability on the partitioning of precipitation between rainfall and snowfall, and how these propagate to spatially distributed estimates of hydrological states and fluxes. VIC lapses grid-averaged air temperature to each elevation band, assigning the same incoming shortwave and longwave radiation, air pressure, relative humidity, and wind speed to all the bands that belong to the same grid cell.

In VIC, snowfall (P_s) at each elevation band is computed following a temperature threshold approach (Andreadis et al., 2009):

$$P_s = \begin{cases} P & T_a \leq T_{min} \\ \dfrac{T_{max} - T_a}{T_{max} - T_{min}} \times P & T_{min} < T_a < T_{max} \\ 0 & T_a \geq T_{max} \end{cases} \quad (2)$$

where P is total precipitation, T_a is air temperature, and T_{min} and T_{max} are parameters.

In this work, we use local air temperature lapse rates. To obtain these, we cluster our basins into three groups (basins 1–3, 4–7, and 8–9 in Figure 1) based on spatial proximity and compute lapse rates using the mean annual temperatures obtained from the grid cells belonging to each cluster. Importantly, these lapse rates are not affected by the configuration of elevation bands, since they are computed from a meteorological product (CR2MET) that assumes flat grid cells. All simulations with elevation bands are performed in full energy balance mode, without horizontal runoff routing. Finally, we decide to use the same VIC parameters found in Section 3.3.2 to isolate the implications of subgrid air temperature distributions from potential compensatory effects that could arise from parameter calibration (e.g., Elsner et al., 2014).

3.3.3. Analysis Framework

We select three continuous periods for analysis based on observed catchment-scale precipitation and runoff: (i) a 5-year wet period, (ii) a 5-year dry period, and (iii) a climatological period that spans April/1982 to March/2015, including (i) and (ii). The choice of wet and dry periods is based upon visual inspection of annual precipitation time series and the calculation of 5-year moving averages of precipitation and runoff. The wet period (April/1982 to March/1987) begins after a long epoch with a persistent negative trend in annual precipitation across semi-arid central Chile (30°–35°S) from the beginning of the twentieth century until the mid-1970s (Quintana & Aceituno, 2012). The dry period (April/2010 to March/2015) covers the first half of the megadrought, when severe annual rainfall deficits (25%–45%) prevailed in central Chile (30°–38°S), diminishing the Andean snowpack and resulting in amplified declines of river flow (up to 90%), reservoir volumes, and groundwater levels (Garreaud et al., 2017).

First, we assess the capability of the benchmark model and each alternative model configuration (i.e., six model configurations in total) to reproduce observed daily runoff, flow duration curves, and runoff seasonality. In this analysis, flow duration curves and runoff seasonality graphs are calculated for the climatological period. We compute the KGE and NSE for modeled runoff at daily and monthly time steps. Additionally, we examine the percent bias for the midsegment slope (%BiasFMS)—which quantifies errors in representing the flashiness (i.e., variability) of runoff—and the low-segment volume (%BiasFLV)—which quantifies errors in baseflow volumes—of the flow duration curves (Yilmaz et al., 2008):

$$\%\mathrm{BiasFMS} = \frac{\left[\log(\mathrm{QS}_{m1}) - \log(\mathrm{QS}_{m2})\right] - \left[\log(\mathrm{QO}_{m1}) - \log(\mathrm{QO}_{m2})\right]}{\left[\log(\mathrm{QO}_{m1}) - \log(\mathrm{QO}_{m2})\right]} \times 100 \tag{3}$$

$$\%\mathrm{BiasFLV} = -1 \times \frac{\sum_{l=1}^{L}\left[\log(\mathrm{QS}_{l}) - \log(\mathrm{QS}_{L})\right] - \sum_{l=1}^{L}\left[\log(\mathrm{QO}_{l}) - \log(\mathrm{QO}_{L})\right]}{\sum_{l=1}^{L}\left[\log(\mathrm{QO}_{l}) - \log(\mathrm{QO}_{L})\right]} \times 100 \tag{4}$$

where QS is the simulated flow (m^3/s), QO is the observed flow (m^3/s), $m1$ and $m2$ are the lowest and highest flow exceedance probabilities (0.2 and 0.7, respectively), and L is the index of the minimum flow.

Then, we compute percent changes between alternative model configurations and the benchmark model results to quantify the effects of adding elevation bands on simulated input/output fluxes and SWE. Specifically, we examine mean annual rainfall, snowfall, runoff, sublimation, snowmelt, and ET, as well as 1 September SWE (SWE 09/01 hereafter) at both catchment and grid cell (i.e., 0.05°) scales. We decide to use SWE 09/01 (instead of other dates) because the snow accumulation season ends (on average) by 1 September along the semiarid Chilean Andes. Accordingly, this variable is used as predictand for statistical models that provide operational seasonal streamflow forecasts in central Chile (Mendoza et al., 2014).

To analyze in detail the effects of snow bands with different vertical discretizations on simulated daily SWE, albedo, cumulative sublimation, and cumulative snowmelt, we select three grid cells with different locations, mean elevations, and elevation ranges within the Mapocho River basin (Figure 3). These comparisons are conducted for water years (WYs) selected from our wet and dry periods to examine the interplay between hydro-climatic conditions and the configuration of elevations bands. We choose the Mapocho River basin for detailed analyses because (a) it has the largest elevation range (>4,400 m) among our case study basins and, therefore, topography is expected to play a key role on hydrology; (b) it has a mixed runoff regime dominated by snowmelt, which makes it an interesting case study to analyze, and (c) it is relevant for water resources planning, since it provides freshwater for populated districts in Santiago de Chile (Alvarez-Garreton et al., 2022).

To identify the most sensitive grid cells and model configurations in terms of snow accumulation, we compare SWE 09/01 (i.e., SWE at the beginning of snowmelt season) obtained from the 200-m configuration and the benchmark, for all WYs (i.e., 33) in the climatological period. We select the 200-m configuration because streamflow performance metrics do not improve considerably when moving from 200- to the 100-m discretization (see details in Section 4.2). We define a grid cell as sensitive if differences in simulated SWE 09/01 with respect to the benchmark model are larger than 10% for >50% of WYs. To seek for controls on different grid cell behavior, we compare the cumulative distribution functions (CDFs) of topographic and climatic attributes (Table 3) obtained from sensitive versus insensitive grid cells. Among the climate descriptors, we include the averaged storm temperature during the accumulation season (T_{storm})—obtained as the mean air temperature for daily

10.1029/2022WR032113

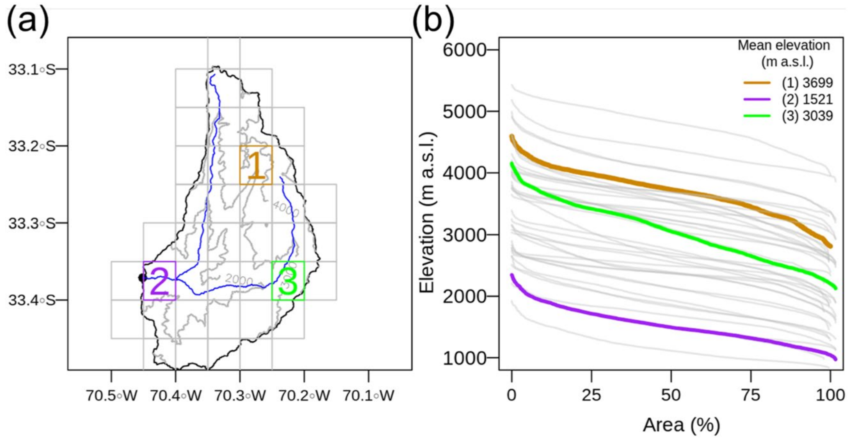

Figure 3. (a) Selected grid cells of the Mapocho River basin; the black dot represents the catchment outlet. (b) Hypsometric curves of the grid cells displayed in panel (a) (represented by gray lines), including the three selected for detailed analysis (highlighted with different colors).

precipitation events throughout April–September—and mean Spring temperature (T_{spring}), obtained as the average temperature over October–December. To compute T_{storm}, we use days when daily precipitation is larger than an arbitrary threshold of 5 mm to avoid artifacts of the gridded product (though the analysis was repeated using a 0 mm threshold, with very similar results). We select T_{storm} and T_{spring} because these are relevant descriptors for liquid/solid precipitation fraction and snowmelt rates, respectively.

We also contrast CDFs of state variables and fluxes simulated with the 200-m model configuration in sensitive versus insensitive grid cells, including rainfall, snowfall, ET, runoff, snowmelt, and maximum SWE. In all these comparisons, we perform Kolmogorov-Smirnov tests and report associated p-values.

4. Results

4.1. Model Evaluation Against Observed Streamflow

Figure 4 compares modeled daily runoff time series against observations for WY 2009/2010 (as an example), as well as mean monthly runoff and daily flow duration curves for the climatological period. The results show small differences between the benchmark model (i.e., no elevation bands) and the alternative model configurations. Adding elevation bands provides a maximum KGE increment of 0.03 for daily streamflow throughout all basins during WY 2009/2010 (see Table 4). All model configurations underestimate daily peak flows during winter (e.g., Figures 4f.1 and 4h.1) and fail to capture streamflow recessions, providing slower (e.g., see Figure 4f.1 between June and August) or faster (e.g., see Figure 4i.1 between July and August) responses compared to observed runoff. In the Palos River basin (Figure 4g.1), there are notable discrepancies in December arising from different vertical discretizations. Figure 4 also shows that all model configurations capture catchment-scale runoff seasonality reasonably well, excepting Estero Arrayán (Figure 4b.2), where rainfall contributions to runoff are underestimated, or the Las Leñas basin (Figure 4d.2), where modeled maximum monthly values are delayed. In some cases, observed monthly values are overestimated (e.g., Pocuro basin, Figure 4a.2) or underestimated (e.g., December–March at the Ñuble basin, Figure 4i.2; near August, Figure 4g.2).

The results for the percent bias in the midsegment slope of the flow duration curves (%BiasFMS, Table 5) show that all model simulations yield flashier responses compared to observed runoff in all basins. When adding elevation bands, %BiasFMS increases in the Pocuro and Arrayán basins compared to the benchmark model, with maximum variations of 2.1% and 3.7% using the 1,000-m configuration, respectively, and these changes do not necessarily correlate with increased vertical resolution. However, elevation bands provide improvements (i.e., decrease in %BiasFMS) in the rest of the basins, ranging from 0.3% for the Claro River basin (200-m configuration) to 8.3% for Las Leñas River basin (200-m configuration).

The incorporation of elevation bands yields reductions in the percent bias in FDC low-segment volume (%BiasFLV, Table 5) in all catchments except the Mapocho River basin. As with %BiasFMS, improvements in %BiasFLV

Table 3
Attributes Considered for Each Grid Cell

Attributes name	Description	Units	Formula
Altitude	Mean elevation	m a.s.l.	–
Range	Difference between maximum and minimum elevation	m	$z_{\max} - z_{\min}$
Aspect	Average grid cell aspect, calculated counterclockwise from east	°	$\tan^{-1}\left(-\frac{dz/dy}{dz/dx}\right)\cdot\frac{180}{\pi}$, where $\left(\frac{dz}{dj}\right)$ is the rate of change in the jth direction
Slope	Mean slope across each grid cell	°	$-\tan^{-1}\left(\sqrt{\left(\frac{dz}{dx}\right)^2+\left(\frac{dz}{dy}\right)^2}\right)\cdot\frac{180}{\pi}$, where $\left(\frac{dz}{dj}\right)$ is the rate of change in the jth direction
Annually averaged storm temperature (T_{storm})	Mean air temperature for daily precipitation events during the accumulation season (April–September)	°C	$\frac{1}{N_{\mathrm{storm}}}\sum_{i=1}^{N_{\mathrm{storm}}} T_{\mathrm{d}}\,[P_{\mathrm{d}} > 5\,\mathrm{mm}]$
Mean spring temperature (T_{spring})	Mean air temperature for spring days (October–December)	°C	$\frac{1}{N_{\mathrm{s}}}\sum_{i=1}^{N_{\mathrm{s}}} T_{\mathrm{d,Spring}}$
Annual precipitation (P)	Annual P for a specific water year	mm/year	$\sum_{i=1}^{N} P_{\mathrm{d}}$
Annual moisture index (I_{m})[a]	Indicates whether climatic conditions are arid (water limited) or humid (energy limited). Ranges from −1 to 1, with negative and positive values for arid and humid conditions, respectively	–	$I_{\mathrm{m}} = \frac{1}{12}\sum_{t=1}^{t=12}\mathrm{MI}(t)$, where $\mathrm{MI}(t) = \begin{cases} 1-\frac{E_{\mathrm{p}}(t)}{P(t)} & P(t) > E_{\mathrm{p}}(t) \\ 0 & P(t) = E_{\mathrm{p}}(t) \\ \frac{P(t)}{E_{\mathrm{p}}(t)}-1 & P(t) < E_{\mathrm{p}}(t) \end{cases}$
Moisture index seasonality ($I_{\mathrm{m,r}}$)[a]	Indicates intra-annual changes in the water/energy budget. Ranges from 0 (no intra-annual changes) to 2 (climate conditions fluctuate between fully arid and fully saturated)	–	$I_{\mathrm{m,r}} = \max(\mathrm{MI}(1,2,\ldots 12)) - \min(\mathrm{MI}(1,2,\ldots 12))$
Fraction of annual precipitation that occurs as snowfall (f_{s})[a]	Ranges from 0 to 1, where 0 indicates no snowfall in a year and 1 that all precipitation occurs as snow	–	$f_{\mathrm{s}} = \frac{\sum_{t=1}^{12} P_{\mathrm{s}}(t)}{\sum_{t=1}^{12} P(t)}$

Note. All calculations are performed using water years (April–March). P_{d} and T_{d} are daily precipitation and daily temperature, respectively. N_{storm} is the number of days within the accumulation season (i.e., April–September, which spans Fall and Winter) when $P_{\mathrm{d}} > 5$ mm. N_{spring} and N are the number of spring (October–December) days and the total number of days in each water year, respectively. MI(t) is a version of the Thornthwaite's moisture index (Willmott & Feddema, 1992). $P(t)$, $P_{\mathrm{s}}(t)$, and $E_{\mathrm{p}}(t)$ are mean monthly precipitation, snowfall, and PET, respectively, for month t.

[a]These climate indices were used in Knoben et al. (2018). It should be noted that the fraction of annual precipitation that occurs as snow (f_{s}) was not calculated as in Knoben et al. (2018), because VIC computes snowfall considering a minimum temperature at which rainfall can occur and a maximum temperature at which snowfall can occur, rather than using a single temperature as threshold.

are not correlated with the vertical resolution, and they range from 0.01% for Pocuro (1,000-m configuration) to 1.03% for Las Leñas (200-m configuration). However, large negative biases in simulated long-term baseflow responses are obtained in some basins (Figures 4c.3, 4d.3, 4e.3, 4g.3, 4h.3, and 4i.3) with all model configurations.

Figure 5 illustrates the sensitivity of KGE to the configuration of elevation bands across basins and analysis periods, for daily (top panels) and monthly (bottom panels) runoff. In general, these results reinforce the idea that adding elevation bands has marginal effects on simulated basin-averaged runoff, yielding KGE improvements (ΔKGE) during the 5-year wet period that range from 0 to 0.05 (Palos basin) for both daily (Figure 5a) and monthly (Figure 5d) time scales. During the 5-year dry period (Figures 5b and 5e), the overall KGE improvement (average from all catchments) is 0.02, with the largest increments obtained for the Palos and Mapocho River basins (although the resulting KGE is still low), and negligible variations (~0.01) in the remaining basins. Interestingly, the improvements in KGE achieved during the wet (dry) period by increasing the vertical discretization in the Claro and Palos River basins (Mapocho River basin) are explained by higher KGE values during the Spring season (not shown).

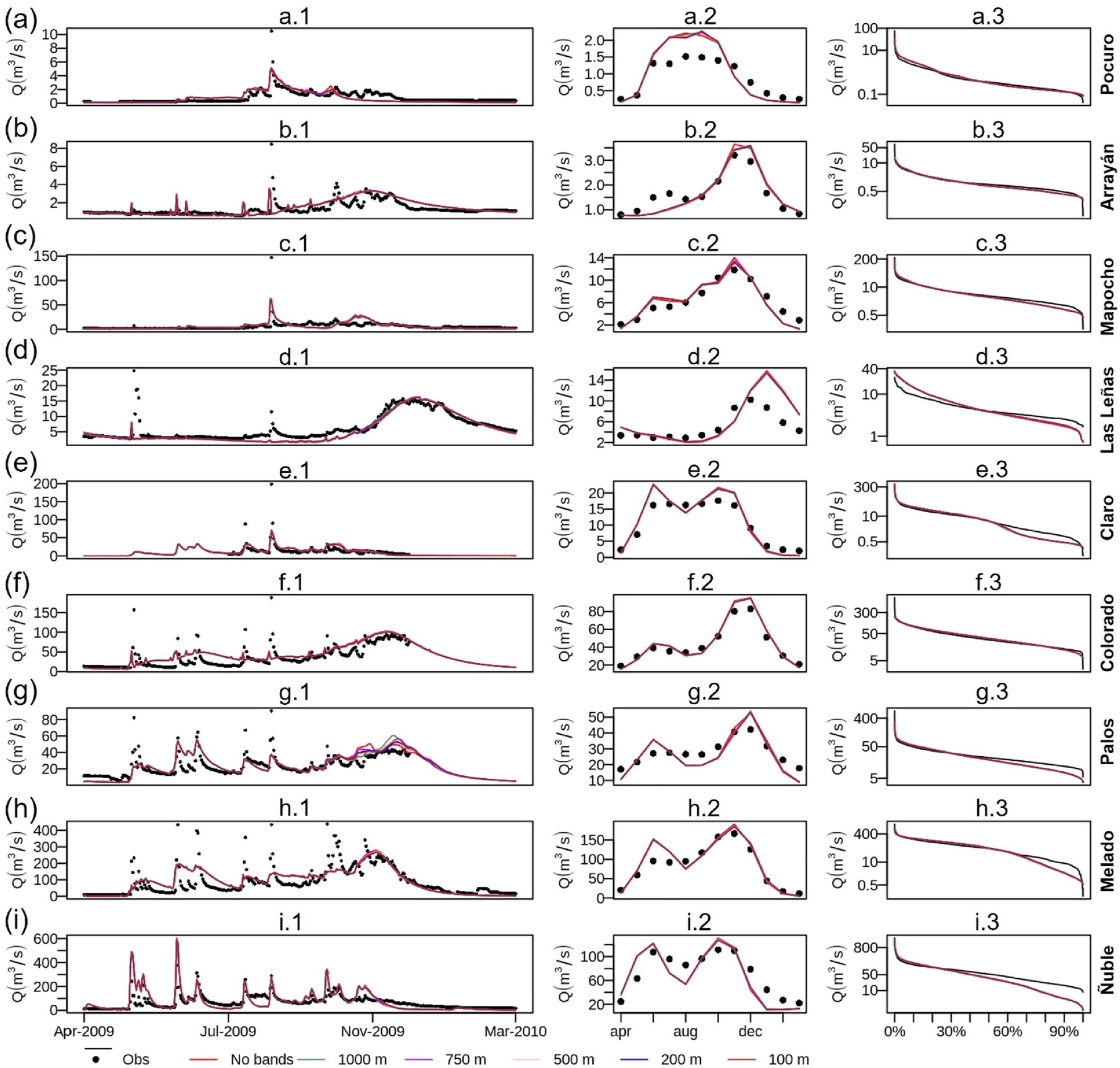

Figure 4. Comparison between simulated and observed runoff (Q) for all basins in terms of daily time series (April/2009 to March/2010, left panels), mean monthly runoff (center panels), and daily flow duration curves (right panels, vertical logarithmic scale). The results in center and right panels correspond to the climatological period. In the left panels, missing dots indicate the absence of runoff measurements.

During the climatological period (Figures 5c and 5f), similar performance metrics are obtained for the 200- and 100-m configurations. For daily runoff simulations (Figure 5c), adding elevation bands provides KGE improvements ranging 0.02–0.03 in Las Leñas and Mapocho basins, and slight KGE reductions (less than 0.01) in the Colorado and Melado basins. KGE values obtained from monthly runoff simulations (Figure 5f) increase between 0.01 and 0.03 in all basins when 200- and 100-m configurations are used.

The results displayed in Figure 5 show that distributing air temperature along elevation bands generally yields slight improvements in streamflow simulations in terms of KGE; however, a higher vertical resolution does not necessarily translate into increased KGE in all basins (e.g., see results for Estero Arrayán in Figures 5a–5c). A noteworthy result from Figure 5 is the constant, larger positive effect on KGE that adding elevation bands provides in the Palos River basin during the wet period compared to the dry period, which may be explained

10.1029/2022WR032113

Table 4
KGE Values for Simulated Daily Runoff—WY 2009/2010

Model configuration	Pocuro	Arrayán	Mapocho	Las Leñas	Claro	Colorado	Palos	Melado	Ñuble
No bands (NB)	0.73	0.58	0.58	0.79	0.51	0.64	0.70	0.69	0.32
1,000 m	0.74	0.58	0.59	0.81	0.51	0.65	0.70	0.69	0.33
750 m	0.74	0.58	0.59	0.79	0.51	0.65	0.70	0.69	0.33
500 m	0.74	0.58	0.61	0.80	0.51	0.65	0.73	0.69	0.34
200 m	0.74	0.59	0.60	0.81	0.51	0.65	0.72	0.68	0.34
100 m	0.74	0.58	0.60	0.81	0.51	0.65	0.72	0.68	0.34

by the linear shape of its hypsometric curve over most of its fractional area (not shown), favoring more evenly distributed areas across elevation bands. More generally, Figure 5 shows that the effects of increased vertical resolution are not necessarily linear, that is, some "coarse" model configurations provide better KGE results than configurations with more elevation bands, yet both configurations are an improvement compared to the benchmark (see, e.g., 750-m configuration results for the Pocuro basin in Figure 5d, and 1,000-m configuration results of the Arrayán basin in Figure 5f). The analysis of KGE components (see Figures S5–S7 in Supporting Information S1) reveals a similar behavior for these metrics, that is, slight variations of results with the choice of snow band configuration during the dry period and changes in both wet and climatological periods. The largest impacts of alternative model configurations are obtained for the α component (Figure S7 in Supporting Information S1), with a moderate reduction.

The results in Figure 5 also reveal model transferability problems toward drier periods. Indeed, the KGE decreases considerably during the dry period in the Pocuro, Palos, and Mapocho River basins. In the Pocuro basin (which is the most arid one), changes in KGE can be explained by a considerable decay in correlation (Figure S5 in Supporting Information S1) from 0.78 to values below (0.91) to 0.2 (0.3) in daily (monthly) simulations, and overestimation in flow volumes ($\beta > 1.6$, Figure S6 in Supporting Information S1), and also in flow variability ($\alpha > 2.5$, Figure S7 in Supporting Information S1), especially at monthly time scales. Similar transferability issues are observed in the Palos and Mapocho River basins, though the decay in KGE is mainly explained by substantial overestimation of streamflow variability during the dry period ($\alpha > 1.8$, Figure S7 in Supporting Information S1), and moderate deterioration of streamflow simulations in terms of timing (Figure S5 in Supporting Information S1) and volumes (Figure S6 in Supporting Information S1).

The effects of distributing air temperature along elevation bands are somewhat different for NSE, for which improvements during the wet and climatological periods are greater than the response of KGE, especially in

Table 5
Model Evaluation Metrics Derived From the Daily Flow Duration Curve (Period April/1982 to March/2015)

Metric	Config.	Pocuro	Arrayán	Mapocho	Las Leñas	Claro	Colorado	Palos	Melado	Ñuble
%BiasFMS	No bands (NB)	15.5	21.6	22.6	53.4	45.8	5.2	52.9	31.2	59.9
	1,000 m	17.6	25.3	22.1	47.3	46.0	4.7	50.1	27.8	57.7
	750 m	16.0	23.2	20.8	46.5	46.1	4.8	50.8	27.4	57.3
	500 m	16.7	23.2	22.3	45.8	45.4	4.7	49.3	25.9	55.8
	200 m	16.9	24.1	22.4	45.1	45.5	4.4	48.4	24.9	56.0
	100 m	17.4	23.9	22.2	45.2	45.4	4.5	47.8	24.8	55.6
%BiasFLV	No bands (NB)	2.0	5.4	6.9	6.5	14.4	0.8	6.3	14.2	16.1
	1,000 m	2.0	5.3	7.2	5.7	14.3	0.8	6.2	13.6	15.9
	750 m	1.9	5.2	6.9	5.6	14.3	0.8	6.2	13.6	15.9
	500 m	2.0	5.2	7.1	5.5	14.2	0.7	6.1	13.4	15.8
	200 m	2.0	5.1	7.0	5.5	14.2	0.7	6.0	13.2	15.7
	100 m	2.0	5.1	7.1	5.5	14.2	0.7	6.0	13.1	15.7

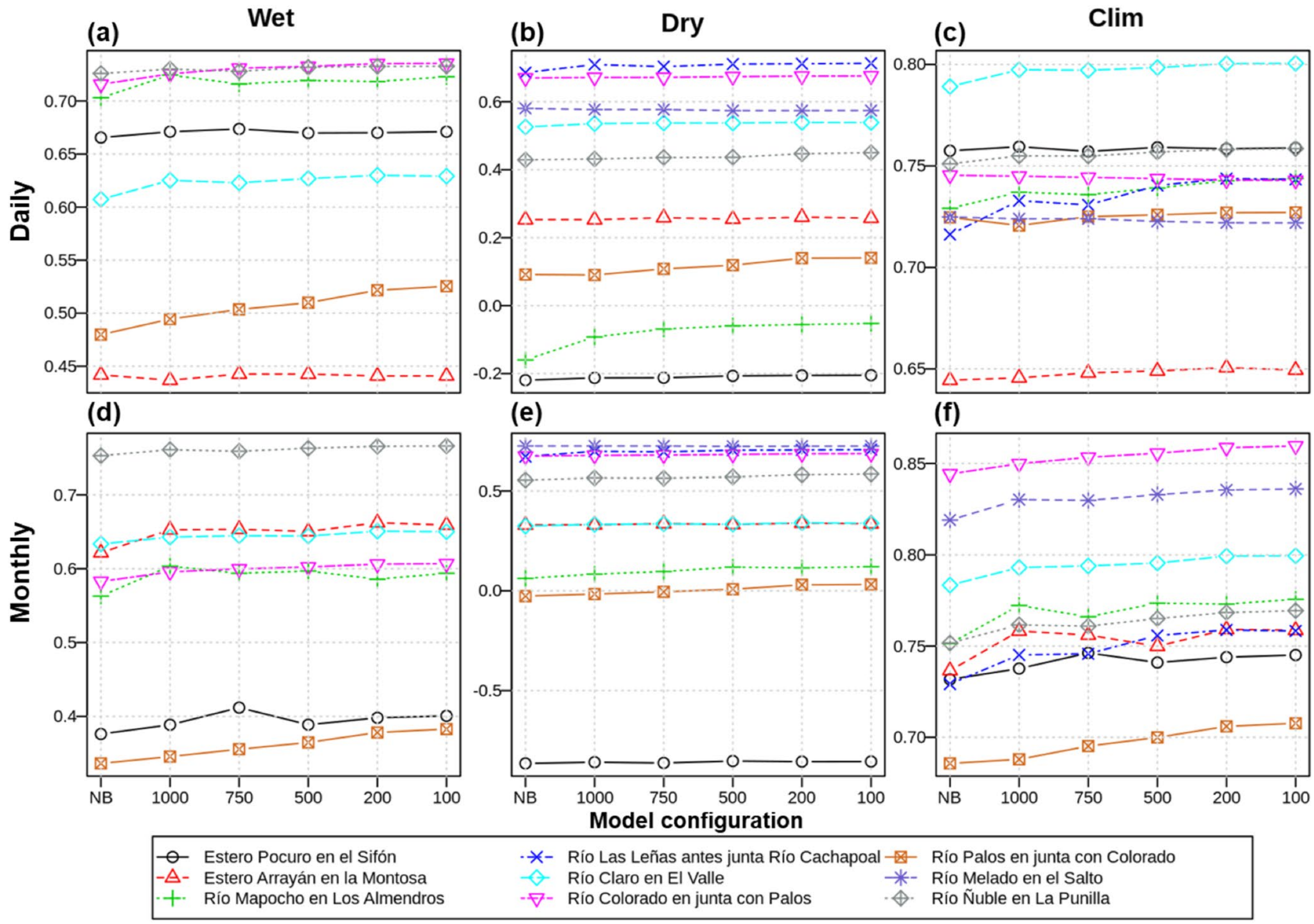

Figure 5. Kling-Gupta efficiency (KGE) results computed with daily (top) and monthly (bottom) runoff, obtained from the benchmark (NB: no bands) and the five alternative model configurations (i.e., using 1,000-, 750-, 500-, 200-, and 100-m elevation bands). Each curve displays individual basin results, and missing basins in some panels indicate the absence of verification (i.e., observed) data for that period.

the Arrayán River basin. Further, negligible changes in NSE are observed during the dry period (Figure S4 in Supporting Information S1). Again, the model performance decays considerably at the Pocuro River basin during the dry period.

4.2. Effects on Mean Annual Fluxes and 1 September SWE

4.2.1. Catchment-Scale Variations

Figure 6 illustrates the effects of adding elevation bands on simulated basin-averaged mean annual fluxes and SWE 09/01. Overall, changes in annual averages are smaller than 5% (with a few exceptions). Differences between alternative configurations are usually smaller than differences between the benchmark and any model configuration with elevation bands, and the effects of increasing the vertical resolution are very small beyond 200-m. Further, variations produced by alternative model configurations are not necessarily proportional to the vertical resolution of elevation bands, and the sign of such impacts in a specific catchment may differ depending on the analysis period.

The alternative model configurations produce slight variations in mean annual runoff, with ~0.15% reductions during the wet and climatological periods in most basins. During the dry period, small reductions (<0.1%) are obtained in the Colorado, Melado, and Ñuble River basins. The Arrayán River basin is the only catchment where the inclusion of elevation bands slightly increases (~0.5%) the mean annual runoff in all analyses. These small variations in mean annual runoff—compared to the other variables displayed in Figure 6—suggest that the similarity in KGE values obtained for daily and monthly runoff with all model configurations (Figure 5) may be

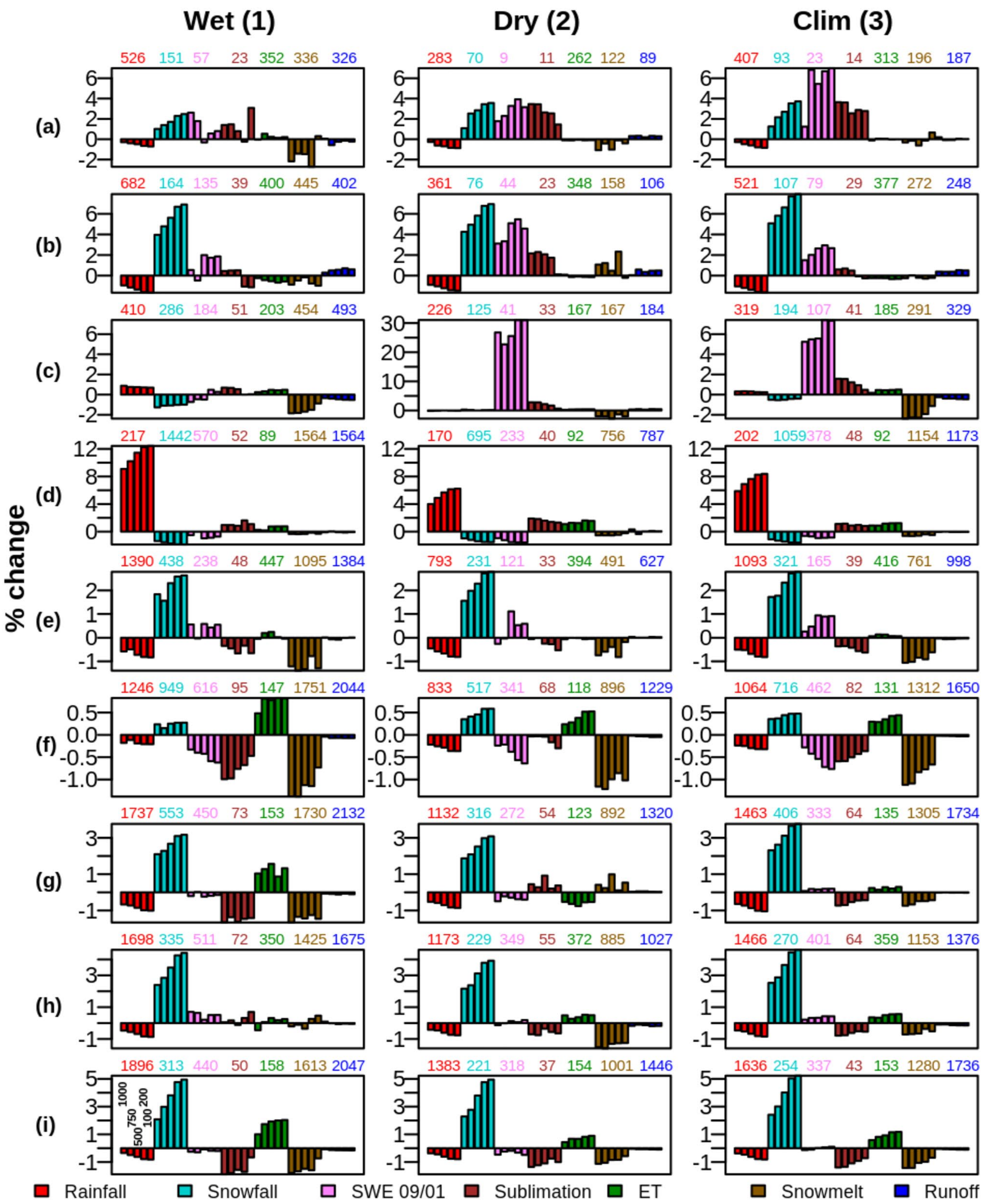

Figure 6. Percent changes (100 × [alternative − benchmark]/benchmark) in simulated basin-averaged mean annual fluxes and snow water equivalent (SWE) 09/01 for different periods (columns) and all case study basins. In each panel, the bars holding the same color represent, from left to right, percent changes for model configurations with 1,000, 750, 500, 200, and 100 m elevation bands (as shown in panel i.1, above the bars with rainfall results). The numbers located over each set of bars indicate the values obtained with the benchmark model (in mm/year for fluxes and mm for SWE 09/01). Note that a different axis range is used for the Mapocho River basin during the dry period (c.2), due to overaccumulation on a grid cell with glacierized area (not shown here) which affects simulated SWE 09/01.

attributed to very different reasons. Indeed, mean annual rainfall decreases in seven catchments (i.e., all basins except Las Leñas and Mapocho) around 0.7%–0.9% during the wet period, as the number of elevation bands increases due to changing the snow-rain partitioning of precipitation. Very similar variations are observed during the dry and climatological periods; even more, the inclusion of more elevation bands also yields less rainfall during the dry period in the Mapocho River basin. Conversely, average increases of 2%–3% in mean annual snowfall are obtained with the alternative model configurations.

The implementation of elevation bands yields mixed variations across catchments in basin-averaged SWE 09/01 with respect to the benchmark model. Negative changes are obtained in Las Leñas and Colorado River basins during all analysis periods; and small (<0.5%) negative variations in SWE 09/01 are obtained in the Palos River basin during the dry period. In the remaining basins, more SWE 09/01 is simulated with the alternative model configurations, and variations depend on the analysis period and vertical discretization.

Interestingly, the results in Figure 6 show that more simulated snowfall does not necessarily yield more SWE 09/01. For example, adding elevation bands increases snowfall in the Colorado River basin in all analysis periods, producing less SWE 09/01 compared to the benchmark model. Additionally, all alternative configurations provide more snowfall in the Pocuro River basin; however, more SWE 09/01 is obtained during the dry period and the climatological period, and less SWE 09/01 during the wet period.

Figure 6 also shows that incorporating subgrid elevation bands generally yields less snowmelt with a few exceptions (i.e., Figures 6b.2 and 6g.2) and mixed variations in annual sublimation amounts. Indeed, elevation bands tend to provide more sublimation in northern, water-limited (i.e., PET/$P > 1$) catchments (e.g., Figures 6a–6d) and generally less sublimation in energy-limited (i.e., PET/$P < 1$) basins. Additionally, part of the rainfall feeds the snowpack, providing liquid water that contributes to increase SWE during the winter season, which explains why VIC produces more annual snowmelt than annual snowfall. For example, the mean annual snowfall obtained with the baseline model at the Pocuro River basin is 93 mm/year, while the mean annual snowmelt for the same period is 196 mm/year.

Slight increases (~0.6%) in simulated basin-averaged ET are obtained with the alternative model configurations during the wet (except Arrayán, with ~0.5% decreases) and climatological periods. During the dry period, the addition of elevation bands yields less simulated ET in four basins (Pocuro, Arrayán, Claro, and Palos).

4.2.2. Intra-Catchment Variability

We now examine intra-catchment variability in changes induced by the alternative model configurations on simulated hydrological variables. Specifically, we assess percent changes (100 × [alternative − benchmark]/benchmark) in simulated mean annual fluxes and SWE 09/01 at each grid cell across the Mapocho River basin (Figure 7). The same figures for the remaining catchments are included in Figures S8–S15 in Supporting Information S1. It can be noted that the effects of elevation bands on mean annual rainfall are more evident in high-elevation areas (over 3,000 m a.s.l.), where larger increments (all computed as the mean from the alternative configurations) are obtained during the wet period (~9% average; Figure 7a) compared to the dry period (~2% average; Figure 7b); additionally, rainfall increments are larger than 20% in some high-elevation grid cells during the wet period. Conversely, the incorporation of elevation bands yields less rainfall in low-elevation grid cells, with declines <5%.

As expected, simulated snowfall increases in grid cells located below 2,500 m a.s.l. when elevation bands are included, with larger increments for higher vertical resolutions. Snowfall variations in low-elevation areas are larger during the wet period using all alternative model configurations, spanning +20%–50%. Further, adding elevation bands in the Mapocho River basin decreases snowfall amounts less than 10% in some grid cells located above 2,500 m a.s.l. The largest variations in SWE 09/01 generally occur below 3,000 m a.s.l., and these are more pronounced during the dry period; however, this behavior is not observed in the rest of the basins (see from Figures S8–S15 in Supporting Information S1). Simulated annual sublimation and snowmelt can be largely affected by the inclusion of elevation bands. Interestingly, the sign and magnitude of snowmelt variations does not necessarily match the spatial patterns of changes in SWE 09/01. Finally, Figure 7 shows that the alternative model configurations do not induce substantial changes in mean annual ET and runoff across the basin of interest, which is also observed in the remaining basins.

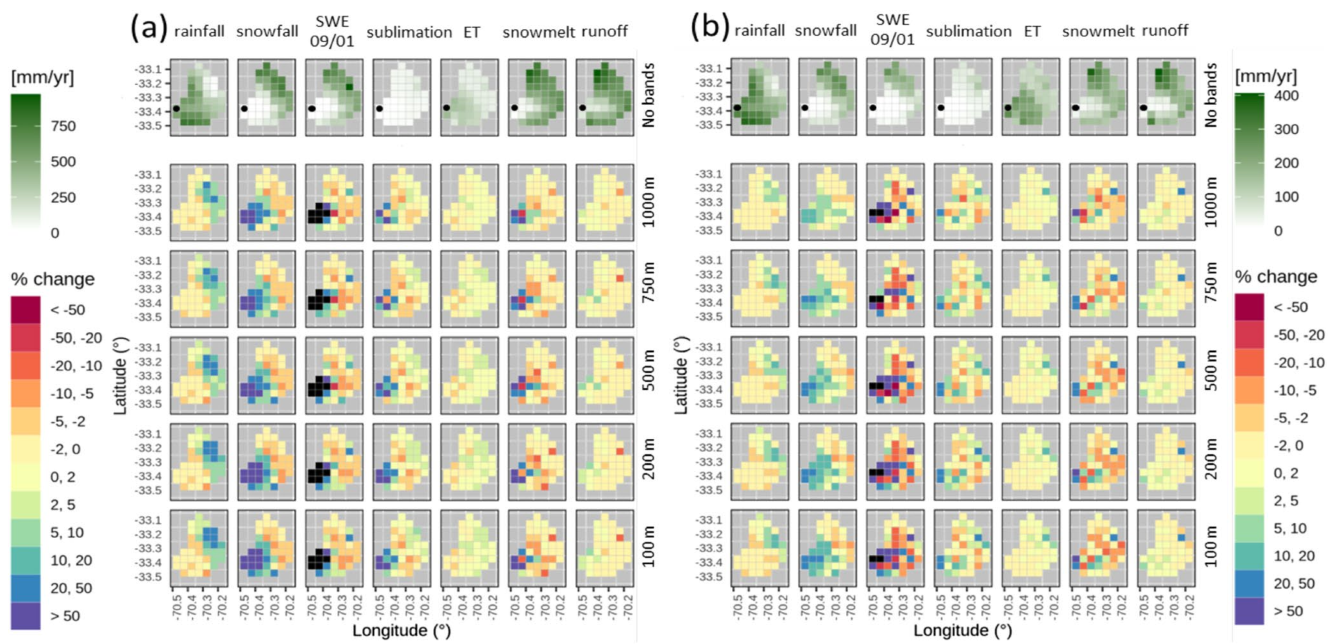

Figure 7. Spatial variability of percent changes (100 × [alternative − benchmark]/benchmark) in grid cell-scale simulated mean annual fluxes and snow water equivalent (SWE) 09/01 at the Mapocho River basin. Results are presented for (a) wet and (b) dry analysis periods. The various columns display, from left to right, results for mean annual rainfall, mean annual snowfall, mean SWE 09/01, mean annual sublimation, mean annual evapotranspiration (ET), mean annual snowmelt, and mean annual runoff. The top row displays results for the benchmark model in mm/year (excepting SWE 09/01, presented in mm), while the remaining rows show results for alternative model configurations (i.e., 1,000, 750, 500, 200, and 100 m elevation bands, from top to bottom). Black tiles indicate grid cells with benchmark model results equal to zero (or unbounded result), and the gray tiles represent grid cells that do not cover any portion of the catchment. The black dot in the top row represents the catchment outlet.

Overall, the main mechanistic explanation for intra-catchment variability seems to be precipitation partitioning. Indeed, the increase in rainfall (and decrease of SWE 09/01) over high-elevation grid cells obtained with the alternative configurations is explained by the appearance of elevation bands that are lower than the mean grid cell elevation, generating areas where air temperature is not cold enough to produce snowfall during precipitation events. Analogously, the increase in snowfall over low-elevation grid cells is explained by the appearance of elevation bands with higher mean altitudes (compared to grid cell averages) when using the alternative configurations. During wet years, changes in sublimation and melt also seem to be related with precipitation partitioning, with an increase (decrease) of these fluxes associated with larger (lower) snow accumulation. However, during dry years, the changes in these variables are less clear and might be related to the specific dynamics of turbulent fluxes at each grid cell.

4.3. Differences in Simulated Daily SWE

We examine simulations of daily SWE and three related variables (albedo, cumulative sublimation, and cumulative snowmelt) in three grid cells of the Mapocho River basin (Figure 3) during WYs 1984 and 2012, characterized by wet and dry conditions, respectively (Figure 8). Model simulations with elevation bands yield less SWE in all grid cells during WY 1984 (wet), and snow disappearance gets delayed in grid cells (2) and (3) compared to the benchmark model. In grid cell (1), this does not happen due to its high mean altitude (3,699 m a.s.l.), yielding snow bands with similar altitudes and, therefore, a similar timing of simulated snow accumulation and melt. During WY 2012 (dry), the alternative model configurations also provide less average SWE than the benchmark model, with specific effects on simulated accumulation and melt events. For example, the 1,000-m configuration in grid cell (1) yields the largest melt rates before October, although it provides the highest SWE compared to the other configurations; in grid cell (2), a precipitation event at the end of July/2012 produces snow accumulation only if elevation bands are considered, even though it gets quickly melted; in grid cell (3), the alternative configurations provide less maximum SWE (~20 mm in mid-June) than the benchmark model, despite they generate earlier (almost 2 weeks) snow accumulation and extend the snow season for more than a week in some cases.

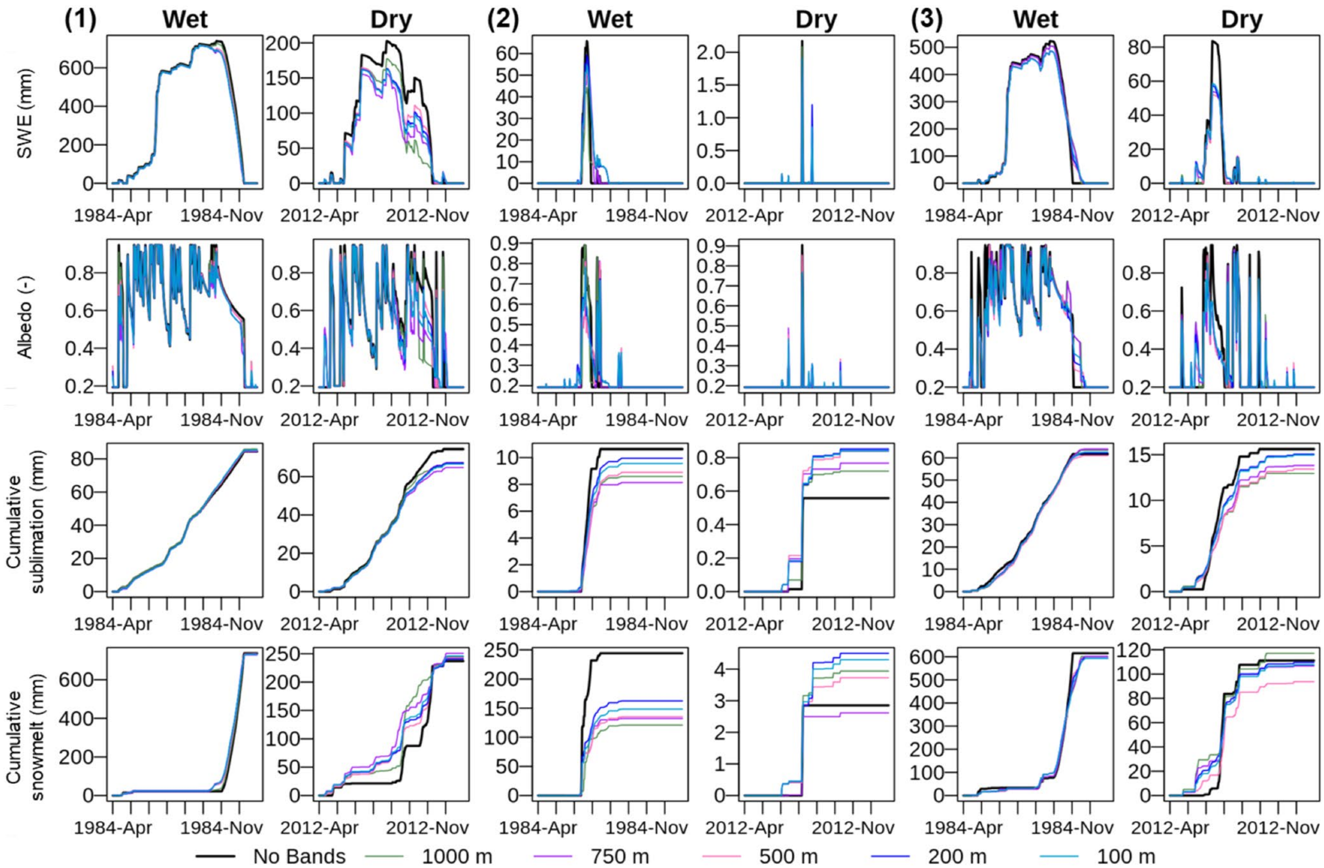

Figure 8. Simulated time series of daily snow water equivalent (SWE), albedo, cumulative sublimation, and cumulative snowmelt for the benchmark model and the alternative model configurations, for the selected grid cells. Panels (1), (2), and (3) correspond to grid cells (1), (2), and (3) in Figure 3, respectively. Each column displays results for a snow season belonging to a wet (WY 1984) and a dry (WY 2012) water year.

Although alternative model configurations yield less SWE in grid cell (1) during WY 2012, lower and earlier snowmelt is obtained compared to the benchmark model, which provides fast, step-like responses.

For the albedo, the largest differences in grid cell (1) are observed in the dry period, especially during the melt season (after September). Around the same date, cumulative sublimation from the alternative configurations begins to depart from the benchmark model results.

Figure 9 displays time series of daily SWE simulated by individual elevation bands (gray lines) in grid cells (1), (2), and (3) (Figures 3.1, 3.2, and 3.3, respectively), using 1,000-m (top panel) and 200-m (bottom panel) configurations. These band widths are selected to illustrate the contrast between a coarse vertical discretization (1,000 m), and the band width beyond which no considerable improvements were obtained in streamflow simulations (200 m). It can be noted that differences in grid cell averaged SWE between the benchmark model (red lines) and alternative configurations (black lines) are mainly attributed to little snow accumulation in low-elevation bands (represented by the lowest gray lines). Indeed, these bands provide the largest departures from the benchmark model because the fraction of precipitation occurring as snowfall is considerably smaller (not shown). The comparison between 1,000- and 200-m configurations shows that adding more elevation bands enhances differences with the benchmark model; for example, the 1,000-m (200-m) configuration yields 25 (39) mm less peak SWE than the benchmark in grid cell (1) during the dry period (Figure 9.1). Further, the 200-m configuration yields larger seasonally averaged SWE than the 1,000-m configuration due to more snow accumulation at high elevations. Increasing the vertical resolution affects the magnitude of simulated SWE, with higher values in October 2012 using the 200-m configuration (Figure 9.1, dry); indeed, the latter configuration provides a ∼50 mm reduction in October 20 SWE compared to the benchmark model, while the 1,000-m configuration reduces SWE for more than 80 mm the same day. This reveals another interesting feature: despite some high-elevation bands

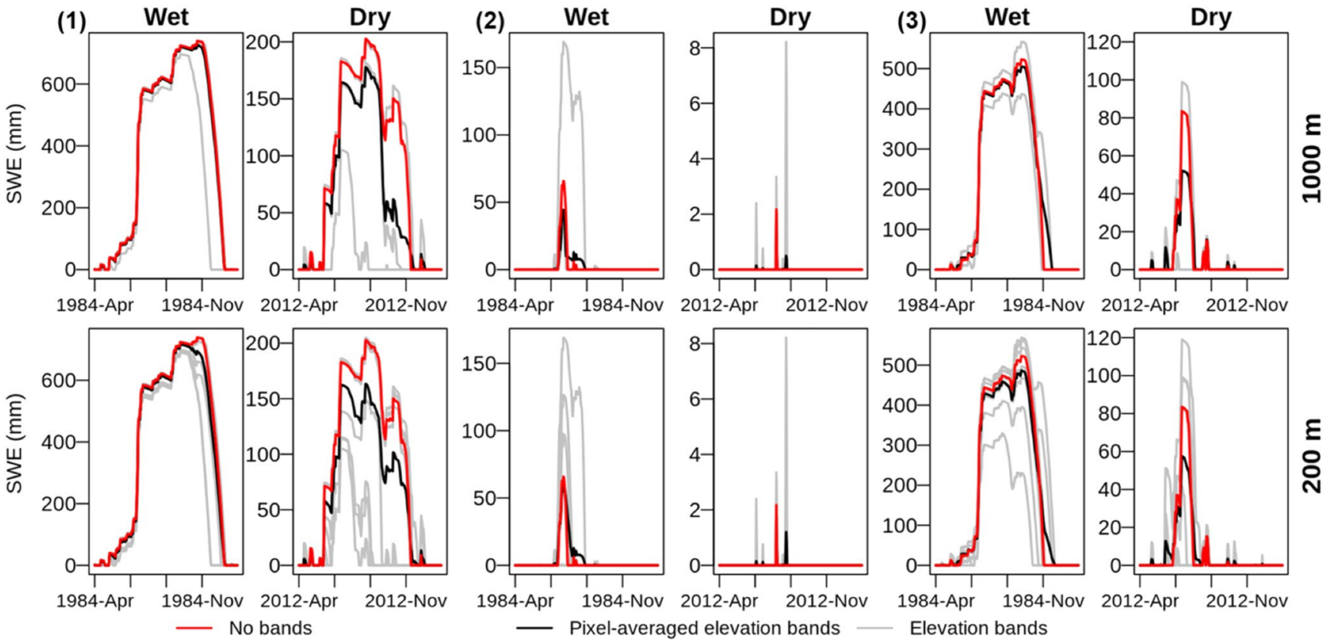

Figure 9. Comparison between simulated time series of daily snow water equivalent (SWE) at the grid cell scale (i.e., 0.05°) using the benchmark model (red line), versus an alternative model configuration (black line) with elevation bands (Δz = 1,000 m, top panel; and Δz = 200 m, bottom panels) for selected grid cells (panels (1), (2), and (3) correspond to grid cells (1), (2), and (3) in Figure 3, respectively). In each panel, the gray lines show simulated daily SWE at all elevation bands contained in the grid cell of interest, with larger SWE associated with higher band-averaged altitudes. Each column displays results for a snow season belonging to a wet (WY 1984) and a dry (WY 2012) water year.

accumulating more SWE than the benchmark model (see gray lines above the red line), this is not translated into increased spatially averaged SWE at the same grid cell, due to their low contributing area.

In the low-elevation grid cell (Figure 9.2), adding elevation bands yields a longer snow season, and the 200-m configuration enables more snow accumulation (compared to 1,000-m), getting closer to the benchmark model results. Finally, the simulations for both (the 200-m) configurations during WY 1984 (WY 2012; after September) in grid cell (3) (Figure 9.3) show that adding higher elevation bands (see the higher gray lines) can delay the occurrence of grid cell averaged snowmelt events. The highest elevation bands start accumulating snow earlier during WY 2012, compared to the benchmark simulation.

4.4. Identification of Sensitive Grid Cells

The results in Figure 7 and Figures S8–S10 in Supporting Information S1 show that adding elevation bands may have large effects on simulated SWE 09/01 in some grid cells, introducing considerable intra-catchment variability. Nevertheless, this variability compensates in such a way that implementing elevation bands yields smaller (or negligible) effects at the basin scale (Figure 10a), compared to the grid cell scale (0.05°) used here (Figure 10b). Hence, we now turn our attention to the question: where does the implementation of elevation bands make a larger difference in simulated SWE? To seek for answers, we examine discrepancies in CDFs of 10 topographic and climate attributes (defined in Section 3.3.3) between sensitive and insensitive grid cells (Figure 11). The results show that sensitive grid cells have lower mean elevations (median of 1,700 m a.s.l.), larger elevation ranges and average slope, and smaller aspect in the range 120–240 (NW-SW) than insensitive ones. Further, sensitive grid cells show higher storm (T_{storm}) and spring (T_{spring}) temperatures, a smaller fraction of precipitation falling as snowfall (f_s), and higher values for annual average moisture index (I_m)—indicating more humid conditions—and the moisture index seasonality ($I_{m,r}$), which reflects more pronounced intra-annual variations in meteorological conditions, switching from fully arid to fully saturated.

Figure 12 displays the CDFs of states and fluxes simulated with 200-m elevation bands in sensitive and insensitive grid cells, showing larger rainfall amounts in sensitive grid cells (median of ~1,500 mm/year) compared to insensitive grid cells (median ~1,250 mm/year); conversely, smaller snowfall amounts (median ~190 mm/year)

10.1029/2022WR032113

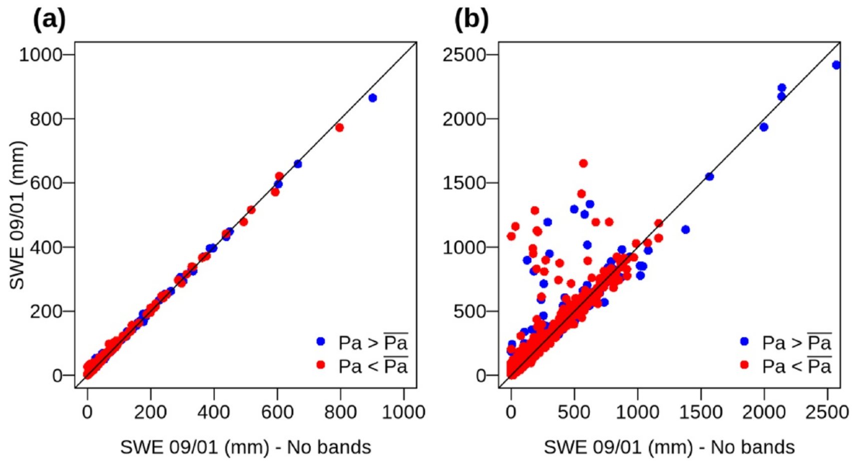

Figure 10. Simulated snow water equivalent (SWE) 09/01 using 200-m elevation bands versus the same variable obtained with the benchmark model at the (a) catchment scale and (b) individual 0.05° grid cells. Each dot indicates results for a specific combination of water year and spatial unit, and each panel comprises results from all the grid cells contained in the nine case study basins. Results are stratified for dry (red) and wet (blue) water years, defined using the mean annual precipitation ($\overline{P_a}$) for the climatological period as threshold.

are seen in sensitive grid cells compared to insensitive grid cells (median ~330 mm/year). Accordingly, lower values of maximum SWE are reached in sensitive grid cells (median ~370 mm) compared to insensitive grid cells (median ~590 mm/year). This behavior is expected given the relatively lower mean elevation of sensitive grid cells (Figure 11). The results for annual snowmelt show large differences in the shape of the CDFs, similar to annual precipitation behavior (Figure 11). The sublimation of sensitive grid cells is higher (median ~60 mm/year) compared to insensitive grid cells (median ~45 mm/year), and the shapes of the CDFs are similar to those of maximum SWE. Annual runoff discrepancies between sensitive and insensitive grid cells are only noticeable for values smaller than 1,600 mm/year, with a relatively larger *p*-value. Finally, we do not find considerable ET differences between sensitive and insensitive grid cells.

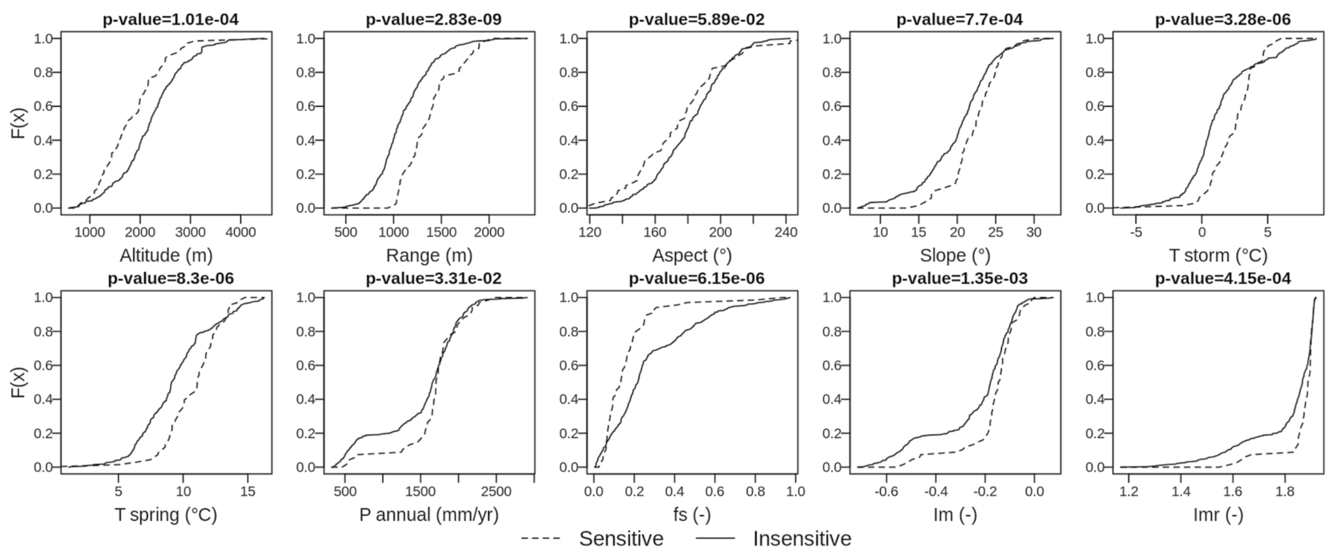

Figure 11. Cumulative distribution functions (CDFs) of selected topographic and hydroclimatic attributes for sensitive versus insensitive grid cells. Aspect values of 180° (90°) represent west (north) facing grid cells. We identify grid cells as sensitive if differences in simulated snow water equivalent (SWE) 09/01 with respect to the benchmark model are larger than 10% for >50% of water years in the climatological period. The *p*-value is obtained from applying the Kolmogorov-Smirnov test between sensitive and insensitive groups. The results were obtained using the 200-m configuration.

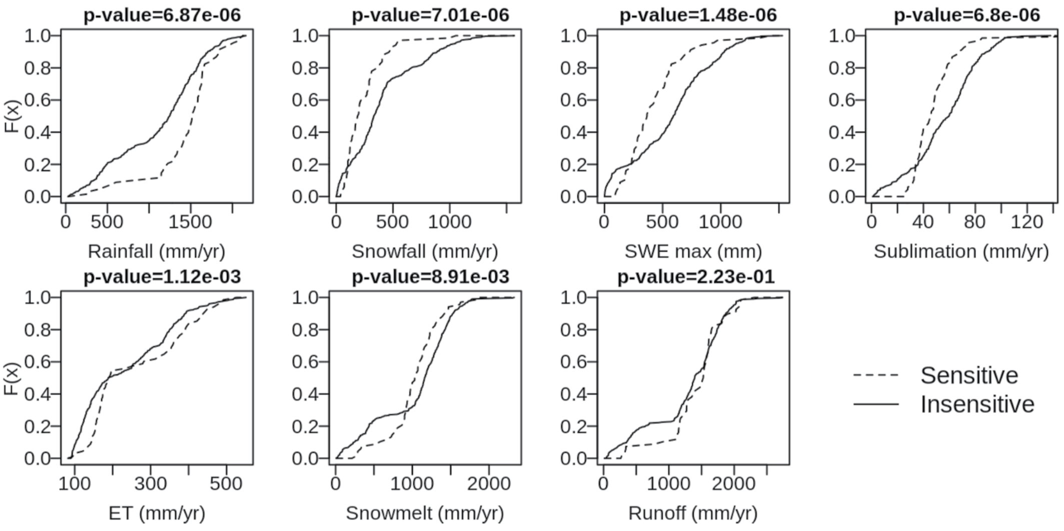

Figure 12. Same as in Figure 11, but for model states and fluxes.

5. Discussion

5.1. Impacts on Streamflow Performance Metrics

The results presented in this paper unveil several implications that the delineation of elevation bands and vertical temperature distributions may have on hydrological characterizations, including streamflow performance metrics. Indeed, the KGE results for daily and monthly streamflow (Table 4) do not differ considerably among the model configurations tested here. The maximum KGE improvement provided by alternative model configurations (compared to the benchmark) is ΔKGE = 0.03 for the Mapocho and Palos River basins, which cannot be considered an improvement in streamflow simulations due to the inclusion of snow bands (Clark et al., 2021). Previous studies have also reported that streamflow efficiency indices become insensitive when the number of elevation bands exceeds a given threshold (e.g., Bhatta et al., 2019; Pradhanang et al., 2011). Further, the small changes in KGE found here suggest a form of model–structure–equifinality (Khatami et al., 2019), since spatial heterogeneities arising from different modeling alternatives compensate to produce very similar values for the same performance metric applied at the catchment scale. This is not observed, however, when analyzing the bias in the FDC midsegment slope (%BiasFMS). For Las Leñas and Melado River basins, the bias reductions (100-m − benchmark) are 8.2% and 6.4%, respectively. A reduction for the same metric is obtained in the remaining basins when comparing the 100-m configuration with the benchmark, excepting the Pocuro and Arrayán River basins. For the FDC low-segment volume (%BiasFLV), small variations (<1.1%) are obtained.

In addition to the equifinality in KGE and NSE, similar errors in simulated flashiness of runoff and baseflow volumes are obtained with the 200- and 100-m configurations for most basins (Table 5), although these can provide different portrayals of the seasonal snowpack evolution (compare simulated time series for 200- and 100-m in Figure 8). In some cases, the 100-m configuration (e.g., %BiasFMS in Las Leñas, Colorado, and Ñuble River basin; %BiasFLV in the Mapocho River basin) yields slightly larger errors than the 200-m configuration, which can be explained by the fact that VIC parameters were not recalibrated for each band configuration. Additionally, a higher vertical resolution provides a more accurate hypsometric curve for a given grid cell, but not necessarily a more realistic representation of topographic heterogeneities, since VIC does not consider local slope and terrain orientation.

5.2. Impacts on Simulated States and Fluxes

Despite the little differences among alternative configurations for KGE (and its components) and NSE, we found notable discrepancies in simulated basin-averaged variables, and spatial differences in rainfall, snowfall, SWE 09/01, sublimation, ET, snowmelt, and runoff compared to the benchmark model (Table 4). In general, smaller variations in simulated hydrological variables are obtained as more elevation bands are added, especially beyond a 200-m vertical resolution, which agrees with past studies (e.g., Bhatta et al., 2019; Essery, 2003; Pradhanang et al., 2011). Interestingly, the direction (i.e., sign) of variations introduced by elevation bands (compared to the benchmark) is not the same for all catchments and hydroclimatic conditions of the analysis period. For example, introducing subgrid temperature distributions contributes to increased sublimation in water-limited (PET/$P > 1$), steep basins with a very small forest fraction (<0.5%), compared to energy-limited basins (PET/$P < 1$). Nevertheless, we did not find a general relationship between hydrological regimes and performance metrics (Figure 5 and Figures S4–S7 in Supporting Information S1) or variations in basin-averaged annual fluxes (Figure 6). However, we noticed that the inclusion of elevation bands in the rainfall-dominated basin (Pocuro, Figure 6a) produces the increase of snowfall, whereas the inclusion of elevation bands in the snow-dominated basin (Las Leñas, Figure 6d) yields an increase of rainfall. These results are similar to those obtained for snow-dominated (high-elevation) and rainfall-dominated (low-elevation) grid cells in the Mapocho basin (Figure 7a), suggesting that vertical temperature distributions along elevation bands enhance the contribution of other fluxes in areas that are mainly dominated by one runoff component, increasing the hydrological heterogeneity within the catchments.

As expected, the partitioning of precipitation into snowfall and rainfall and simulated daily SWE can vary considerably when vertical heterogeneity in air temperature is included, and the effects generally increase with vertical resolution. Such heterogeneity causes differences in snow accumulation across elevation bands, decreasing spatially averaged peak SWE in each grid cell, and delaying snow cover depletion (Figure 9). This aligns well with the findings of Essery (2003), who concluded that the aggregated model (equivalent to our benchmark model) was unable to represent winter melt at low elevations and delayed spring melt at high elevations. Other studies have also highlighted the role of subgrid heterogeneity for more realistic SWE calculations, and therefore for improved snowmelt estimates (e.g., Clark et al., 2011; DeBeer & Pomeroy, 2017). Our results also show that low-elevation bands accumulate less SWE and melt earlier, in agreement with observations reported by Tong et al. (2008) for a watershed in western Canada, while the highest elevation bands yield lower melt rates, reducing the snow cover depletion rate (i.e., snow lasts longer). Such differences can be explained by changes in the energy balance (specifically, sensible and latent heat fluxes, Figures S16–S24 in Supporting Information S1) since, in our configuration, precipitation is spatially uniform in each grid cell for all model configurations.

A novel contribution of our study is the identification of climatic and topographic controls defining where it is more important to distribute air temperature along elevation bands. Our results show that the impacts for snowpack simulations are substantial in more humid grid cells, with a relatively smaller fraction of precipitation falling as snow (due to higher temperatures and lower elevation) and a more pronounced seasonality in meteorological conditions. Additionally, elevation range and spatially averaged slope also play a key role. It should be noted, however, that the emergence of topographic features different than elevation—and hence not explicitly considered in VIC—as relevant attributes to define subgrid representations of air temperature simply reflects the influence of horizontal topographic gradients in the development of CR2MET. Indeed, such gradients are included as predictors in the regression equations that distribute precipitation and temperature in space (Juan P. Boisier 2022, personal communication).

5.3. Limitations and Future Work

The results presented here depend on selected hydrological model structure, as well as related deficiencies in terms of process representations. In particular, VIC does not incorporate an aquifer at the bottom of the soil column, nor lateral exchange of fluxes between grid cells. In terms of subgrid variability, the model relies on hypsometric curves to represent orographic heterogeneities, ignoring other topographic features. Further, VIC does not have a mechanism to redistribute vegetation and soil attributes to each elevation band; that is, the same vegetation classes and their fractions, and the soil parameters associated with a specific grid box are assigned to each elevation band. Nevertheless, topography-related heterogeneities in vegetation and soil properties can also affect hydrologic model simulations (Hao et al., 2022).

A key limitation of this study is that subgrid variability in precipitation was not incorporated (Grusson et al., 2015; Pradhanang et al., 2011). Hence, future work could expand these analyses to account for orographic controls on precipitation. Moreover, snow accumulation on steep terrain does depend not only on orographic gradients but also on wind speed, wind direction, and slope orientations, which might vary strongly with elevation. Another limitation of VIC meteorological forcings is that each band uses radiative fluxes estimated at the corresponding grid cell using MTCLIM, instead of estimating these variables for each band using adjusted air temperature.

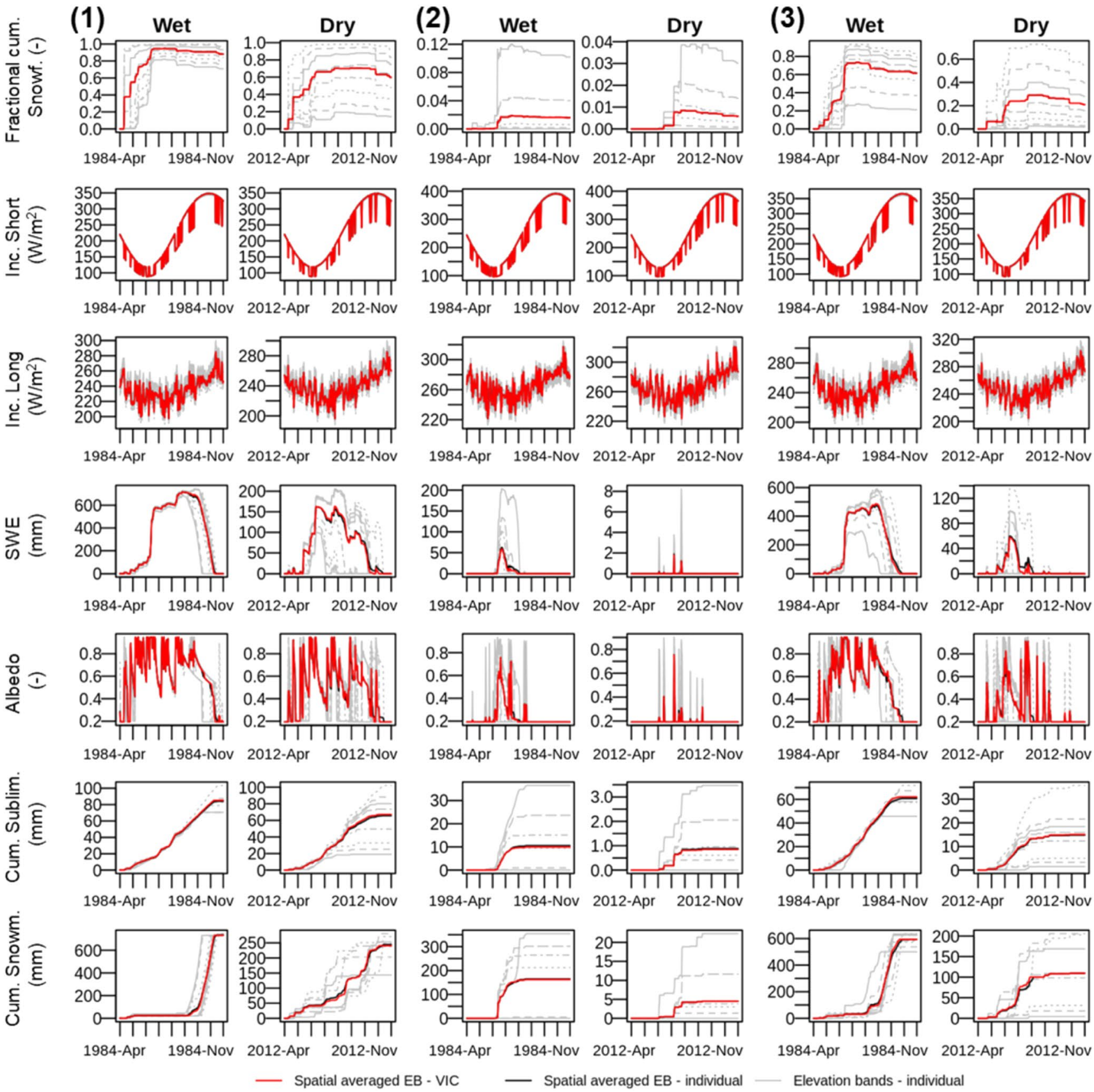

Figure 13. Simulated time series of fractional cumulative snowfall (computed as the ratio between cumulative snowfall and cumulative precipitation), incoming shortwave radiation, incoming longwave radiation, daily snow water equivalent (SWE), albedo, cumulative sublimation, and cumulative snowmelt for grid cell averages obtained from the following model configurations: (1) subgrid variability in temperature along 200-m elevation bands (i.e., red lines); and (2) subgrid variability in air temperature, incoming shortwave radiation and incoming longwave radiation along the same bands. The gray lines show the results for individual elevation bands using the latter configuration. The results in panels (1), (2), and (3) correspond to grid cells (1), (2), and (3) in Figure 3, respectively. Each column displays results for a snow season belonging to a wet (water year [WY] 1984) and a dry (WY 2012).

Nevertheless, this approximation is not far from what would be obtained if incoming shortwave and longwave radiation were also distributed with elevation using the empirical algorithms of MTCLIM. Figure 13 displays a comparison of incoming radiation fluxes and simulated snowpack variables obtained from (a) a model implementation with subgrid variability only for temperature along 200-m elevation bands (EB-VIC) and (b) an additional experiment considering subgrid variability in air temperature and incoming shortwave and longwave radiation along the same bands (EB-Individual). The results show that (a) grid-averaged simulated time series of radiation fluxes are nearly identical; (b) SWE simulations are very similar, with the largest differences between EB-VIC and EB-individual during the ablation season; and (c) slight differences are obtained for simulated albedo, cumulative sublimation, and cumulative snowmelt. Moving beyond the elevation band approach, subgrid parameterizations could be considered to capture topographic effects on radiative fluxes (e.g., Lee et al., 2011), including topographic shadow and reflection to improve the simulations of surface energy fluxes (e.g., Hao et al., 2021, 2022). Moreover, the strategy to delineate snow bands should prioritize a proper representation of SWE at altitudes with the largest areas and high snow accumulation (Helfricht et al., 2012) and, therefore, the effectiveness of irregular spatial discretization based on other topographic variables than elevation such as slope and aspect (e.g., the local approach implemented by Tesfa & Leung, 2017) should be tested.

Despite the results presented in this paper are only valid for a sample of snow-influenced basins, these are located along a pronounced hydroclimatic gradient in the extratropical Andes, which provides diversity in terms of annual hydroclimatology and seasonal hydrological regimes. Additionally, the selected basins encompass a diverse sample of 399 grid cells in terms of climatic and topographic descriptors (Figure 11), enabling to draw robust conclusions regarding the factors that define sensitive grid cells to vertical temperature distributions and, therefore, freezing level estimates in mountain, snow-influenced environments. Future studies could expand the analyses presented here to other snow climates (e.g., Raleigh et al., 2015; Sturm et al., 1995), including more sophisticated approaches to represent subgrid heterogeneities (e.g., Hao et al., 2021; Hazenberg et al., 2015; L. Huang et al., 2022; Swenson et al., 2019; Tesfa & Leung, 2017).

6. Conclusions

We have examined the hydrological implications of representing subgrid air temperature variability in hydrologic modeling through elevation bands, in nine basins located along the western slopes of the Andes Cordillera. Specifically, we implemented five alternative model configurations in the VIC macroscale hydrological model, with elevation bands of 1,000, 750, 500, 200, and 100 m interval to distribute air temperature, and compared their results against a benchmark model (i.e., model without elevation bands) in terms of streamflow simulations, mean annual fluxes, and SWE 09/01, and daily SWE simulations in a suite of grid cells located across the Mapocho River basin. Finally, we analyzed possible physical and climatic characteristics that define those grid cells where elevation bands are more impactful on SWE estimates. The results show that, although the incorporation of elevation bands does not appreciably affect model performance in terms of the KGE for daily and monthly streamflow, it does affect other fluxes and SWE at the catchment scale and the intra-basin variability of simulated variables, suggesting a form of model–structure–equifinality. Other findings are as follows:

- Distributing air temperature along elevation bands yields larger effects in the partitioning of precipitation into rainfall and snowfall, for both catchment and grid cell scales during the wet period (WYs 1982–1986) compared to the dry period. Additionally, differences in ET and runoff between the alternative model configurations and the benchmark are also more pronounced during the wet period, although not as evident as the case of rainfall and snowfall. On the other hand, impacts of vertical discretization on SWE 09/01 are comparatively more relevant during dry periods.
- Adding elevation bands generally yields less basin-averaged snowmelt and more (less) catchment-scale sublimation across water-limited (energy-limited) basins.
- The magnitude of variations in simulated hydrological variables induced by elevation bands is not proportional to the vertical discretization or number of elevation bands adopted.
- Adding elevation bands affects the duration of snow cover with the highest bands holding snow for a longer period and yields earlier snow accumulation during the WY compared to the benchmark model.
- SWE 09/01 is generally more affected by elevation bands in grid cells with relatively lower mean altitude, and thus higher T_{storm}/T_{spring}, elevation ranges >1,000 m, steep slopes (>15°), and annual precipitation amounts <1,000 mm with larger intra-annual variations in wetness conditions.

Data Availability Statement

The VIC code; formatted meteorological forcing data; global, soil, and vegetation parameter files; and elevation band files used here for all model configurations and case study basins are publicly available on Zenodo (https://doi.org/10.5281/zenodo.7080219). The streamflow data used for model calibration and evaluation were obtained from the CAMELS-CL data set (Alvarez-Garreton et al., 2018).

Acknowledgments

This research was partially supported by the supercomputing infrastructure of the NLHPC (ECM-02). Pablo A. Mendoza and Nicolás Vásquez received support from Fondecyt Project 11200142; Pablo A. Mendoza was also supported by CONICYT/PIA Project AFB220002. Álvaro Ayala is supported by Fondecyt Postdoctoral Project 3190732. The authors thank Ximena Vargas for her suggestions on earlier versions of this manuscript, Juan Pablo Boisier for his help with the CR2MET data set, and three anonymous reviewers, whose feedback greatly improved the manuscript.

References

Abbaspour, K. C., Yang, J., Maximov, I., Siber, R., Bogner, K., Mieleitner, J., et al. (2007). Modelling hydrology and water quality in the pre-alpine/alpine Thur watershed using SWAT. *Journal of Hydrology*, *333*(2–4), 413–430. https://doi.org/10.1016/j.jhydrol.2006.09.014

Abdulla, F. A., Lettenmaier, D. P., Wood, E. F., & Smith, J. A. (1996). Application of a macroscale hydrologic model to estimate the water balance of the Arkansas–Red River Basin. *Journal of Geophysical Research*, *101*(D3), 7449–7459. https://doi.org/10.1029/95JD02416

Addor, N., & Melsen, L. A. (2019). Legacy, rather than adequacy, drives the selection of hydrological models. *Water Resources Research*, *55*, 378–390. https://doi.org/10.1029/2018WR022958

Alvarez-Garreton, C., Boisier, J. P., & Marinao, R. (2022). La crítica situación del agua potable en la Región Metropolitana. Retrieved from https://www.cr2.cl/analisis-cr2-la-critica-situacion-del-agua-potable-en-la-region-metropolitana/

Alvarez-Garreton, C., Mendoza, P. A., Pablo Boisier, J., Addor, N., Galleguillos, M., Zambrano-Bigiarini, M., et al. (2018). The CAMELS-CL dataset: Catchment attributes and meteorology for large sample studies—Chile dataset. *Hydrology and Earth System Sciences*, *22*(11), 5817–5846. https://doi.org/10.5194/hess-22-5817-2018

Andreadis, K. M., & Lettenmaier, D. P. (2006). Assimilating remotely sensed snow observations into a macroscale hydrology model. *Advances in Water Resources*, *29*(6), 872–886. https://doi.org/10.1016/j.advwatres.2005.08.004

Andreadis, K. M., Storck, P., & Lettenmaier, D. P. (2009). Modeling snow accumulation and ablation processes in forested environments. *Water Resources Research*, *45*, W05429. https://doi.org/10.1029/2008WR007042

Arola, A., & Lettenmaier, D. P. (1996). Effects of subgrid spatial heterogeneity on GCM-scale land surface energy and moisture fluxes. *Journal of Climate*, *9*(6), 1339–1349. https://doi.org/10.1175/1520-0442(1996)009<1339:EOSSHO>2.0.CO;2

Arora, M., Singh, P., Goel, N. K., & Singh, R. D. (2008). Climate variability influences on hydrological responses of a large Himalayan basin. *Water Resources Management*, *22*(10), 1461–1475. https://doi.org/10.1007/s11269-007-9237-1

Baez-Villanueva, O. M., Zambrano-Bigiarini, M., Mendoza, P. A., McNamara, I., Beck, H. E., Thurner, J., et al. (2021). On the selection of precipitation products for the regionalisation of hydrological model parameters. *Hydrology and Earth System Sciences*, *25*(11), 5805–5837. https://doi.org/10.5194/hess-25-5805-2021

Bajracharya, A. R., Bajracharya, S. R., Shrestha, A. B., & Maharjan, S. B. (2018). Climate change impact assessment on the hydrological regime of the Kaligandaki Basin, Nepal. *Science of the Total Environment*, *625*, 837–848. https://doi.org/10.1016/j.scitotenv.2017.12.332

Bandaragoda, C., Tarboton, D. G., & Woods, R. A. (2004). Application of TOPNET in the distributed model intercomparison project. *Journal of Hydrology*, *298*(1–4), 178–201. https://doi.org/10.1016/j.jhydrol.2004.03.038

Barnett, T. P., Adam, J. C., & Lettenmaier, D. P. (2005). Potential impacts of a warming climate on water availability in snow-dominated regions. *Nature*, *438*(7066), 303–309. https://doi.org/10.1038/nature04141

Beck, H. E., Pan, M., Lin, P., Seibert, J., van Dijk, A. I. J. M., & Wood, E. F. (2020). Global fully distributed parameter regionalization based on observed streamflow from 4,229 headwater catchments. *Journal of Geophysical Research: Atmospheres*, *125*, e2019JD031485. https://doi.org/10.1029/2019JD031485

Bhatta, B., Shrestha, S., Shrestha, P. K., & Talchabhadel, R. (2019). Evaluation and application of a SWAT model to assess the climate change impact on the hydrology of the Himalayan River Basin. *Catena*, *181*, 104082. https://doi.org/10.1016/j.catena.2019.104082

Bohn, T. J., Livneh, B., Oyler, J. W., Running, S. W., Nijssen, B., & Lettenmaier, D. P. (2013). Global evaluation of MTCLIM and related algorithms for forcing of ecological and hydrological models. *Agricultural and Forest Meteorology*, *176*, 38–49. https://doi.org/10.1016/j.agrformet.2013.03.003

Bohn, T. J., Sonessa, M. Y., & Lettenmaier, D. P. (2010). Seasonal hydrologic forecasting: Do multimodel ensemble averages always yield improvements in forecast skill? *Journal of Hydrometeorology*, *11*(6), 1358–1372. https://doi.org/10.1175/2010JHM1267.1

Boisier, J. P., Alvarez-Garretón, C., Cepeda, J., Osses, A., Vásquez, N., & Rondanelli, R. (2018). CR2MET: A high-resolution precipitation and temperature dataset for hydroclimatic research in Chile. In *EGU General Assembly Conference Abstracts* (p. 19739).

C3S, & Copernicus Climate Change Service (C3S). (2017). ERA5: Fifth generation of ECMWF atmospheric reanalyses of the global climate. Retrieved from https://cds.climate.copernicus.eu/cdsapp%23%21/home

Chen, F., Barlage, M., Tewari, M., Rasmussen, R., Jin, J., Lettenmaier, D., et al. (2014). Modeling seasonal snowpack evolution in the complex terrain and forested Colorado Headwaters region: A model intercomparison study. *Journal of Geophysical Research: Atmospheres*, *119*, 13795–13819. https://doi.org/10.1002/2014JD022167

Cherkauer, K. A., & Lettenmaier, D. P. (2003). Simulation of spatial variability in snow and frozen soil. *Journal of Geophysical Research*, *108*(D22), 8858. https://doi.org/10.1029/2003JD003575

Clark, M. P., Hendrikx, J., Slater, A. G., Kavetski, D., Anderson, B., Cullen, N. J., et al. (2011). Representing spatial variability of snow water equivalent in hydrologic and land-surface models: A review. *Water Resources Research*, *47*, W07539. https://doi.org/10.1029/2011WR010745

Clark, M. P., Nijssen, B., & Luce, C. H. (2017). An analytical test case for snow models. *Water Resources Research*, *53*, 909–922. https://doi.org/10.1002/2016WR019672

Clark, M. P., Vogel, R. M., Lamontagne, J. R., Mizukami, N., Knoben, W. J. M., Tang, G., et al. (2021). The abuse of popular performance metrics in hydrologic modeling. *Water Resources Research*, *57*, e2020WR029001. https://doi.org/10.1029/2020WR029001

DeBeer, C. M., & Pomeroy, J. W. (2017). Influence of snowpack and melt energy heterogeneity on snow cover depletion and snowmelt runoff simulation in a cold mountain environment. *Journal of Hydrology*, *553*, 199–213. https://doi.org/10.1016/j.jhydrol.2017.07.051

Dee, D. P., Uppala, S. M., Simmons, A. J., Berrisford, P., Poli, P., Kobayashi, S., et al. (2011). The ERA-Interim reanalysis: Configuration and performance of the data assimilation system. *Quarterly Journal of the Royal Meteorological Society*, *137*(656), 553–597. https://doi.org/10.1002/qj.828

Demaria, E. M. C., Roundy, J. K., Wi, S., & Palmer, R. N. (2016). The effects of climate change on seasonal snowpack and the hydrology of the Northeastern and Upper Midwest United States. *Journal of Climate*, *29*(18), 6527–6541. https://doi.org/10.1175/JCLI-D-15-0632.1

DGA. (2017). *Actualización del balance hídrico nacional, SIT N°417*. Ministerio de Obras Públicas, Dirección General de Aguas, División de Estudios y Planificación.

Duan, Q. Y., Gupta, V. K., & Sorooshian, S. (1993). Shuffled Complex Evolution approach for effective and efficient global minimization. *Journal of Optimization Theory and Applications*, *76*(3), 501–521. https://doi.org/10.1007/BF00939380

Elsner, M. M., Gangopadhyay, S., Pruitt, T., Brekke, L. D., Mizukami, N., & Clark, M. P. (2014). How does the choice of distributed meteorological data affect hydrologic model calibration and streamflow simulations? *Journal of Hydrometeorology*, *15*(4), 1384–1403. https://doi.org/10.1175/JHM-D-13-083.1

Essery, R. (2003). Aggregated and distributed modelling of snow cover for a high-latitude basin. *Global and Planetary Change*, *38*(1–2), 115–120. https://doi.org/10.1016/S0921-8181(03)00013-4

Fontaine, T. A., Cruickshank, T. S., Arnold, J. G., & Hotchkiss, R. H. (2002). Development of a snowfall–snowmelt routine for mountainous terrain for the soil water assessment tool (SWAT). *Journal of Hydrology*, *262*(1–4), 209–223. https://doi.org/10.1016/S0022-1694(02)00029-X

Garreaud, R., Alvarez-Garreton, C., Barichivich, J., Pablo Boisier, J., Christie, D., Galleguillos, M., et al. (2017). The 2010–2015 megadrought in central Chile: Impacts on regional hydroclimate and vegetation. *Hydrology and Earth System Sciences*, *21*(12), 6307–6327. https://doi.org/10.5194/hess-21-6307-2017

Garreaud, R., Boisier, J. P. P., Rondanelli, R., Montecinos, A., Sepúlveda, H. H. H., & Veloso-Aguila, D. (2019). The central Chile mega drought (2010–2018): A climate dynamics perspective. *International Journal of Climatology*, *40*, 1–19. https://doi.org/10.1002/joc.6219

Gericke, O. J., & Smithers, J. C. (2014). Revue des méthodes d'évaluation du temps de réponse d'un bassin versant pour l'estimation du débit de pointe. *Hydrological Sciences Journal*, *59*(11), 1935–1971. https://doi.org/10.1080/02626667.2013.866712

Grusson, Y., Sun, X., Gascoin, S., Sauvage, S., Raghavan, S., Anctil, F., & Sáchez-Pérez, J. M. (2015). Assessing the capability of the SWAT model to simulate snow, snow melt and streamflow dynamics over an alpine watershed. *Journal of Hydrology*, *531*, 574–588. https://doi.org/10.1016/j.jhydrol.2015.10.070

Gupta, H. V., Kling, H., Yilmaz, K. K., & Martinez, G. F. (2009). Decomposition of the mean squared error and NSE performance criteria: Implications for improving hydrological modelling. *Journal of Hydrology*, *377*(1–2), 80–91. https://doi.org/10.1016/j.jhydrol.2009.08.003

Habets, F., Etchevers, P., Golaz, C., Leblois, E., Ledoux, E., Martin, E., et al. (1999). Simulation of the water budget and the river flows of the Rhone basin. *Journal of Geophysical Research*, *104*(D24), 31145–31172. https://doi.org/10.1029/1999JD901008

Haddeland, I., Matheussen, B. V., & Lettenmaier, D. P. (2002). Influence of spatial resolution on simulated streamflow in a macroscale hydrologic model. *Water Resources Research*, *38*(7), 291–2910. https://doi.org/10.1029/2001WR000854

Hamman, J. J., Nijssen, B., Bohn, T. J., Gergel, D. R., & Mao, Y. (2018). The variable infiltration capacity model version 5 (VIC-5): Infrastructure improvements for new applications and reproducibility. *Geoscientific Model Development*, *11*(8), 3481–3496. https://doi.org/10.5194/gmd-11-3481-2018

Hao, D., Bisht, G., Gu, Y., Lee, W. L., Liou, K. N., & Leung, L. R. (2021). A parameterization of sub-grid topographical effects on solar radiation in the E3SM land model (version 1.0): Implementation and evaluation over the Tibetan plateau. *Geoscientific Model Development*, *14*(10), 6273–6289. https://doi.org/10.5194/gmd-14-6273-2021

Hao, D., Bisht, G., Huang, M., Ma, P. L., Tesfa, T., Lee, W. L., et al. (2022). Impacts of sub-grid topographic representations on surface energy balance and boundary conditions in the E3SM land model: A case study in Sierra Nevada. *Journal of Advances in Modeling Earth Systems*, *14*, e2021MS002862. https://doi.org/10.1029/2021MS002862

Hartman, M. D., Baron, J. S., Lammers, R. B., Cline, D. W., Band, L. E., Liston, G. E., & Tague, C. (1999). Simulations of snow distribution and hydrology in a mountain basin. *Water Resources Research*, *35*(5), 1587–1603. https://doi.org/10.1029/1998WR900096

Hazenberg, P., Fang, Y., Broxton, P., Gochis, D., Niu, G. Y., Pelletier, J. D., et al. (2015). A hybrid-3D hillslope hydrological model for use in Earth system models. *Water Resources Research*, *51*, 8218–8239. https://doi.org/10.1002/2014WR016842

Helfricht, K., Schöber, J., Seiser, B., Fischer, A., Stötter, J., & Kuhn, M. (2012). Snow accumulation of a high alpine catchment derived from LiDAR measurements. *Advances in Geosciences*, *32*, 31–39. https://doi.org/10.5194/adgeo-32-31-2012

Hirabayashi, Y., Döll, P., & Kanae, S. (2010). Global-scale modeling of glacier mass balances for water resources assessments: Glacier mass changes between 1948 and 2006. *Journal of Hydrology*, *390*(3–4), 245–256. https://doi.org/10.1016/j.jhydrol.2010.07.001

Houle, E. S., Livneh, B., & Kasprzyk, J. R. (2017). Exploring snow model parameter sensitivity using Sobol variance decomposition. *Environmental Modelling & Software*, *89*, 144–158. https://doi.org/10.1016/j.envsoft.2016.11.024

Huang, L., Zhang, S., Niu, G. Y., Wei, N., Yuan, H., Wei, Z., et al. (2022). A catchment-based hierarchical spatial tessellation approach to a better representation of land heterogeneity for hyper-resolution land surface modeling. *Water Resources Research*, *58*, e2021WR031589. https://doi.org/10.1029/2021WR031589

Huang, M., Hou, Z., Leung, L. R., Ke, Y., Liu, Y., Fang, Z., & Sun, Y. (2013). Uncertainty analysis of runoff simulations and parameter identifiability in the community land model: Evidence from MOPEX basins. *Journal of Hydrometeorology*, *14*(6), 1754–1772. https://doi.org/10.1175/JHM-D-12-0138.1

Hungerford, R. (1989). *MTCLIM: A Mountain Microclimate Simulation Model* (p. 414). US Department of Agriculture, Forest Service, Intermountain Research Station.

IPCC. (2021). Assessment Report 6 Climate Change 2021: The physical science basis.

Islam, S. u., Déry, S. J., & Werner, A. T. (2017). Future climate change impacts on snow and water resources of the Fraser River basin, British Columbia. *Journal of Hydrometeorology*, *18*(2), 473–496. https://doi.org/10.1175/jhm-d-16-0012.1

Kang, D. H., Shi, X., Gao, H., & Déry, S. J. (2014). On the changing contribution of snow to the hydrology of the Fraser River basin, Canada. *Journal of Hydrometeorology*, *15*(4), 1344–1365. https://doi.org/10.1175/JHM-D-13-0120.1

Khatami, S., Peel, M. C., Peterson, T. J., & Western, A. W. (2019). Equifinality and flux mapping: A new approach to model evaluation and process representation under uncertainty. *Water Resources Research*, *55*, 8922–8941. https://doi.org/10.1029/2018WR023750

Knoben, W. J. M., Woods, R. A., & Freer, J. E. (2018). A quantitative hydrological climate classification evaluated with independent streamflow data. *Water Resources Research*, *54*, 5088–5109. https://doi.org/10.1029/2018WR022913

Lee, W. L., Liou, K. N., & Hall, A. (2011). Parameterization of solar fluxes over mountain surfaces for application to climate models. *Journal of Geophysical Research*, *116*, D01101. https://doi.org/10.1029/2010JD014722

Lehning, M., Völksch, I., Gustafsson, D., Nguyen, T. A., Stähli, M., & Zappa, M. (2006). ALPINE3D: A detailed model of mountain surface processes and its application to snow hydrology. *Hydrological Processes*, *20*(10), 2111–2128. https://doi.org/10.1002/hyp.6204

Li, D., Wrzesien, M. L., Durand, M., Adam, J., & Lettenmaier, D. P. (2017). How much runoff originates as snow in the western United States, and how will that change in the future? *Geophysical Research Letters*, *44*, 6163–6172. https://doi.org/10.1002/2017GL073551

Liang, X., Lettenmaier, D. P., Wood, E. F., & Burges, S. J. (1994). A simple hydrologically based model of land surface water and energy fluxes for general circulation models. *Journal of Geophysical Research*, *99*(D7), 14415–14428. https://doi.org/10.1029/94JD00483

Liang, X., Wood, E. F., & Lettenmaier, D. P. (1996). Surface soil moisture parameterization of the VIC-2L model: Evaluation and modification. *Global and Planetary Change*, *13*(1–4), 195–206. https://doi.org/10.1016/0921-8181(95)00046-1

Liston, G., & Sturm, M. (1998). A snow-transport model for complex terrain. *Journal of Glaciology*, *44*(148), 498–516. https://doi.org/10.3189/s0022143000002021

Livneh, B., & Badger, A. M. (2020). Drought less predictable under declining future snowpack. *Nature Climate Change*, *10*(5), 452–458. https://doi.org/10.1038/s41558-020-0754-8

López-Moreno, J. I., Pomeroy, J. W., Revuelto, J., & Vicente-Serrano, S. M. (2013). Response of snow processes to climate change: Spatial variability in a small basin in the Spanish Pyrenees. *Hydrological Processes*, *27*(18), 2637–2650. https://doi.org/10.1002/hyp.9408

Markstrom, S. L., Niswonger, R. G., Regan, R. S., Prudic, D. E., & Barlow, P. M. (2008). GSFLOW—Coupled ground-water and surface-water flow model based on the integration of the precipitation–runoff modeling system (PRMS) and the modular ground-water flow model (MODFLOW-2005). Methods.

Marshall, A. M., Link, T. E., Abatzoglou, J. T., Flerchinger, G. N., Marks, D. G., & Tedrow, L. (2019). Warming alters hydrologic heterogeneity: Simulated climate sensitivity of hydrology-based microrefugia in the snow-to-rain transition zone. *Water Resources Research*, *55*, 2122–2141. https://doi.org/10.1029/2018WR023063

Mendoza, P. A., Rajagopalan, B., Clark, M. P., Cortés, G., & McPhee, J. (2014). A robust multimodel framework for ensemble seasonal hydroclimatic forecasts. *Water Resources Research*, *50*, 6030–6052. https://doi.org/10.1002/2014WR015426

Mendoza, P. A., Shaw, T. E., McPhee, J., Musselman, K. N., Revuelto, J., & MacDonell, S. (2020). Spatial distribution and scaling properties of Lidar-derived snow depth in the extratropical Andes. *Water Resources Research*, *56*, e2020WR028480. https://doi.org/10.1029/2020WR028480

Minder, J. R., Mote, P. W., & Lundquist, J. D. (2010). Surface temperature lapse rates over complex terrain: Lessons from the Cascade Mountains. *Journal of Geophysical Research*, *115*, D14122. https://doi.org/10.1029/2009JD013493

Mote, P. W., Hamlet, A. F., Clark, M. P., & Lettenmaier, D. P. (2005). Declining mountain snowpack in Western North America. *Bulletin of the American Meteorological Society*, *86*(1), 39–49. https://doi.org/10.1175/BAMS-86-1-39

Nash, J., & Sutcliffe, J. (1970). River flow forecasting through conceptual models part I—A discussion of principles. *Journal of Hydrology*, *10*(3), 282–290. https://doi.org/10.1016/0022-1694(70)90255-6

Newman, A. J., Clark, M. P., Winstral, A., Marks, D., & Seyfried, M. (2014). The use of similarity concepts to represent sub-grid variability in land-surface models: Case study in a snowmelt dominated watershed. *Journal of Hydrometeorology*, *15*(5), 1717–1738. https://doi.org/10.1175/JHM-D-13-038.1

Newman, A. J., Mizukami, N., Clark, M. P., Wood, A. W., Nijssen, B., & Nearing, G. (2017). Benchmarking of a physically based hydrologic model. *Journal of Hydrometeorology*, *18*(8), 2215–2225. https://doi.org/10.1175/JHM-D-16-0284.1

Nijssen, B., Lettenmaier, D. P., Liang, X., Wetzel, S. W., & Wood, E. F. (1997). Streamflow simulation for continental-scale river basins. *Water Resources Research*, *33*(4), 711–724. https://doi.org/10.1029/96WR03517

Nijssen, B., Schnur, R., & Lettenmaier, D. P. (2001). Global retrospective estimation of soil moisture using the variable infiltration capacity land surface model, 1980–93. *Journal of Climate*, *14*(8), 1790–1808. https://doi.org/10.1175/1520-0442(2001)014<1790:GREOSM>2.0.CO;2

Pradhanang, S. M., Anandhi, A., Mukundan, R., Zion, M. S., Pierson, D. C., Schneiderman, E. M., et al. (2011). Application of SWAT model to assess snowpack development and streamflow in the Cannonsville watershed, New York, USA. *Hydrological Processes*, *25*(21), 3268–3277. https://doi.org/10.1002/hyp.8171

Quintana, J., & Aceituno, P. (2012). Changes in the rainfall regime along the extratropical west coast of South America (Chile): 30–43°S. *Atmósfera*, *25*(1), 1–22.

Ragettli, S., Cortés, G., McPhee, J., & Pellicciotti, F. (2014). An evaluation of approaches for modelling hydrological processes in high-elevation, glacierized Andean watersheds. *Hydrological Processes*, *28*(23), 5674–5695. https://doi.org/10.1002/hyp.10055

Raleigh, M. S., Lundquist, J. D., & Clark, M. P. (2015). Exploring the impact of forcing error characteristics on physically based snow simulations within a global sensitivity analysis framework. *Hydrology and Earth System Sciences*, *19*(7), 3153–3179. https://doi.org/10.5194/hess-19-3153-2015

Rasmussen, R., Ikeda, K., Liu, C., Gochis, D., Clark, M., Dai, A., et al. (2014). Climate change impacts on the water balance of the Colorado Headwaters: High-resolution regional climate model simulations. *Journal of Hydrometeorology*, *15*(3), 1091–1116. https://doi.org/10.1175/JHM-D-13-0118.1

Schneider, D., & Molotch, N. P. (2016). Real-time estimation of snow water equivalent in the Upper Colorado River Basin using MODIS-based SWE Reconstructions and SNOTEL data. *Water Resources Research*, *52*, 7892–7910. https://doi.org/10.1002/2016WR019067

Sepúlveda, U. M., Mendoza, P. A., Mizukami, N., & Newman, A. J. (2022). Revisiting parameter sensitivities in the variable infiltration capacity model across a hydroclimatic gradient. *Hydrology and Earth System Sciences*, *26*(13), 3419–3445. https://doi.org/10.5194/hess-26-3419-2022

Sturm, M., Holmgren, J., & Liston, G. E. (1995). A seasonal snow cover classification system for local to global applications. *Journal of Climate*, *8*(5), 1261–1283. https://doi.org/10.1175/1520-0442(1995)008<1261:ASSCCS>2.0.CO;2

Swenson, S. C., Clark, M., Fan, Y., Lawrence, D. M., & Perket, J. (2019). Representing intrahillslope lateral subsurface flow in the community land model. *Journal of Advances in Modeling Earth Systems*, *11*, 4044–4065. https://doi.org/10.1029/2019MS001833

Tachikawa, T., Hato, M., Kaku, M., & Iwasaki, A. (2011). Characteristics of ASTER GDEM version 2. In *International Geoscience and Remote Sensing Symposium (IGARSS)* (pp. 3657–3660). https://doi.org/10.1109/IGARSS.2011.6050017

Tesfa, T. K., & Leung, L. Y. R. (2017). Exploring new topography-based subgrid spatial structures for improving land surface modeling. *Geoscientific Model Development*, *10*(2), 873–888. https://doi.org/10.5194/gmd-10-873-2017

Tesfa, T. K., Li, H. Y., Leung, L. R., Huang, M., Ke, Y., Sun, Y., & Liu, Y. (2014). A subbasin-based framework to represent land surface processes in an Earth system model. *Geoscientific Model Development*, *7*(3), 947–963. https://doi.org/10.5194/gmd-7-947-2014

Tong, J., Déry, S., & Jackson, P. (2008). Topographic control of snow distribution in an alpine watershed of western Canada inferred from spatially-filtered MODIS snow products. *Hydrology and Earth System Sciences Discussions*, *5*(4), 2347–2371. https://doi.org/10.5194/hessd-5-2347-2008

Vásquez, N., Cepeda, J., Gómez, T., Mendoza, P. A., Lagos, M., Boisier, J. P., et al. (2021). Catchment-scale natural water balance in Chile. In *Water resources of Chile* (pp. 189–208). https://doi.org/10.1007/978-3-030-56901-3_9

Vicuña, S., Garreaud, R. D., & McPhee, J. (2011). Climate change impacts on the hydrology of a snowmelt driven basin in semiarid Chile. *Climatic Change*, *105*(3–4), 469–488. https://doi.org/10.1007/s10584-010-9888-4

Vicuña, S., Vargas, X., Boisier, J. P., Mendoza, P. A., Gómez, T., Vásquez, N., & Cepeda, J. (2021). Impacts of climate change on water resources in Chile. In *Water Resources of Chile* (Vol. *13*, pp. 347–363). https://doi.org/10.1007/978-3-030-56901-3_19

Willmott, C. J. J., & Feddema, J. J. J. (1992). A more rational climatic moisture index. *The Professional Geographer*, *44*(1), 84–88. https://doi.org/10.1111/j.0033-0124.1992.00084.x

10.1029/2022WR032113

Xiao, M., Mahanama, S. P. P., Xue, Y., Chen, F., & Lettenmaier, D. P. P. (2021). Modeling snow ablation over the mountains of the western United States: Patterns and controlling factors. *Journal of Hydrometeorology*, *22*(2), 297–311. https://doi.org/10.1175/JHM-D-19-0198.1

Yeste, P., García-Valdecasas Ojeda, M., Gámiz-Fortis, S. R., Castro-Díez, Y., & Esteban-Parra, M. J. (2020). Integrated sensitivity analysis of a macroscale hydrologic model in the north of the Iberian Peninsula. *Journal of Hydrology*, *590*, 125230. https://doi.org/10.1016/j.jhydrol.2020.125230

Yilmaz, K. K., Gupta, H. V., & Wagener, T. (2008). A process-based diagnostic approach to model evaluation: Application to the NWS distributed hydrologic model. *Water Resources Research*, *44*, W09417. https://doi.org/10.1029/2007WR006716

Younas, W., Hay, R. W., MacDonald, M. K., Islam, S. U., & Déry, S. J. (2017). A strategy to represent impacts of subgrid-scale topography on snow evolution in the Canadian Land Surface Scheme. *Annals of Glaciology*, *58*(75), 1–10. https://doi.org/10.1017/aog.2017.29

Zhao, Y., Feng, D., Yu, L., Wang, X., Chen, Y., Bai, Y., et al. (2016). Detailed dynamic land cover mapping of Chile: Accuracy improvement by integrating multi-temporal data. *Remote Sensing of Environment*, *183*, 170–185. https://doi.org/10.1016/j.rse.2016.05.016